Catalytic performance of supported Ni in the hydrodesulfurization of dibenzothiophene

Rodrigo Valderrama-Zapata,[a] Julieth T. García-Sánchez,[a] Omar J. Vargas-Montañez,[a] Sergio A. Rincón-Ortiz,[b] Iván D. Mora-Vergara,[a] David Pérez-Martínez,[c] Edgar M. Morales-Valencia,[a] Víctor G. Baldovino-Medrano*[a,b]

[a] Centro de Investigaciones en Catálisis (CICAT)
Universidad Industrial de Santander
Parque Tecnológico Guatiguará, km 2 vía Guatiguará, El Refugio, Piedecuesta (Santander), 681011, Colombia
E-mail: vicbaldo@uis.edu.co

[b] Laboratorio Central de Ciencia de Superficies (SurfLab)
Universidad Industrial de Santander
Parque Tecnológico Guatiguará, km 2 vía Guatiguará, El Refugio, Piedecuesta (Santander), 681011, Colombia

[c] Centro de Innovación y Tecnología (ICP)
Ecopetrol S.A.
km 7 vía Piedecuesta (Santander), A.A. 4185, Colombia.

Abstract: To reduce pollution, sulfur, nitrogen, and other heteroatoms are removed from fuels by hydrotreatment (HDT). Conventional HDT catalysts are based on Ni-MoS_2 phases dispersed over γ-Al_2O_3. Despite the myriad of papers studying these catalysts, it is somehow surprising to learn that the role of Ni in these catalysts is not yet fully understood. Most literature considers that Ni is either converted to some form of catalytically inactive nickel sulfide or that it mixes with MoS_2 to act as a strong catalytic promoter. In this work, we focused on analyzing whether well dispersed supported nickel nanoparticles can be active in the hydrodesulfurization of dibenzothiophene; one of the most refractory molecules composing diesel and marine fuels. We dispersed nickel using the principles of the strong electrostatic adsorption (SEA) method over silica (~neutral acidity), γ-Al_2O_3 (Lewis acidity), H^+-Y zeolite (Brönsted-Lewis acidity), and microporous-mesoporous H^+-Y zeolite (similar Brönsted-Lewis acidity than its microporous counterpart). The results showed that Ni nanoparticles are catalytically active in the hydrodesulfurization of DBT and that zeolites provide them with long term stability. In addition, using SEA impregnation and providing mesoporosity to the zeolite improved the catalytic performance. Overall, we demonstrate that Ni nanoparticles may behave in the same manner as noble metals such as Pt, Pd, and Ir behave in hydrodesulfurization. We discuss some of probable reasons for such a behavior and remark on the role of Ni in hydrotreatment.

Introduction

Hydrotreating (HDT) cleans fuels by reducing their contents of sulfur, oxygen, nitrogen, and metals such as iron, nickel, and vanadium.[1,2] The process removes ~90% of the above-mentioned pollutants from the liquid fractions of petroleum. Among the multiple reactions that occur during hydrotreating, hydrodesulfurization (HDS) is usually the focus of attention [3–6] given the toxicity of SO_x and its role in the formation of acid rain that harms ecosystems and even urban landscapes.[7–9]

Research on the hydrodesulfurization of heavy oil cuts remains an active field [10,11] since, on the one hand, the demand for fuels such as diesel and jet is still growing worldwide as driven by increasing population in developing countries,[4,12] and, on the other hand, the technologies associated with the process and with catalysts design have found applications in fields such as the production of biofuels,[13] the production of green hydrogen,[14] and fuel cells.[15] In the case of the design of catalysts, there is still much to be learned concerning the relationship between the structure of the catalytic phases and their reactivity towards complex hetero-polycyclic aromatic structures such as dibenzothiophenes.[16–21]

The hydrodesulfurization of dibenzothiophene is a very informative model reaction. Dibenzothiophenes react via two reaction routes over hydrodesulfurization catalysts. One is the direct desulfurization (DDS) route and the other is mediated by the hydrogenation of one of the aromatic rings (HYD) of the molecule before the breakage of its C-S bond.[16,18,19,21–26]

The direct desulfurization of dibenzothiophene is kinetically dominant over conventional γ-Al_2O_3 supported Ni-MoS_2 and Co-MoS_2 catalysts and even over unconventional noble metal promoted MoS_2 catalysts.[26–35] Accordingly, it is generally agreed that MoS_2 is the active phase of the catalysts and that secondary metals such as Ni, Co, and even noble metals essentially act as promoters of the MoS_2. However, the role and functionalities of the metallic promoters is still not fully understood despite extensive experimental [26–34,36,37][38,39] and theoretical efforts.[40–44] A usual conception of the field is that metallic promoters are in a sulfided state during hydrodesulfurization.[45,46] This is based on the pioneering studies of Pecoraro and Chianelli on the reactivity of transition metal sulfides.[47] However, multiple studies have shown that when metallic phases are tested under standard hydrodesulfurization conditions, part of their structure remains in a reduced state and that sulfidation is partly reversible.[48–55] Therefore, reduced metallic moieties can act as active sites for hydrodesulfurization. In the case of nickel, some works show that part of it could remain in metallic state within the structure of a mixed Ni-MoS_2 phase.[28,56] Furthermore, it was recently reported that hydrogen reduced Ni/Al_2O_3 catalysts are active for the hydrodesulfurization of thiophene (a much less refractory compound) at 370 °C, 3 MPa, and an LHSV of 10 h^{-1}.[57]

One of the issues of nickel catalysts is said to be the formation of inactive phases with the catalytic support. In the case of alumina, which is one of the most used support in technical catalysts,[58,59] nickel forms $NiAl_2O_4$ aluminates under typical

synthesis conditions; namely, conventional impregnation of aqueous solutions of nickel nitrate at natural pH and further thermal treatment by roasting at 500 °C.[3] This species have not been found in nickel based catalysts when supports such as silica,[60,61] activated carbon,[45,62] or zeolites[63–69] are used.

Earlier reports by Brooks *et al*.[63,70,71] showed how nickel exchanged mordenite zeolites, Zeolon 900, can do hydrodesulfurization.[63,70,71] According to the reported data, ion exchange led to the deposition of ~3.0 wt.% nickel that formed a distribution of crystallites on mordenite where ~25 – 53% were located outside the nanopores of the zeolite and had particle sizes ranging from 0.2 to 30 nm and ~47 – 75% of the nickel was found as crystallites whose size was lower than 0.2 nm. The produced catalysts were in-situ reduced under H_2 flow and then sulfided inside a fixed-bed reactor with a mixture of a solution of CS_2 and H_2 before testing them in the hydrotreating of a mixture of a naphtha fuel and thiophene at 300 °C, 0.1 MPa, and using various liquid hourly space velocities. The synthesized catalysts were active in the studied reaction and promoted secondary hydrogenation reactions that favored hydrodesulfurization. Afterwards, Davidova *et al*.[64] studied the behavior of nickel ion exchanged Y zeolites in the hydrodesulfurization of diethylsulfide at 250 – 310 °C and atmospheric pressure. In contrast to the works of Brooks *et al*.,[63,70,71] these authors pre-treated their catalysts by reducing them under hydrogen flow. The synthesized catalysts hydrogenolized diethylsulfide more efficiently than parent monometallic molybdenum catalysts. On the other hand, Welters *et al*.[66] compared the properties of Y zeolite supported presulfided nickel catalysts in the hydrodesulfurization of thiophene (400 °C, 0.1 MPa) synthesized by ion exchange and impregnation. The authors highlighted the contribution of the acidity of the zeolites to the catalytic behavior and also showed that the synthesis method may change the location of nickel in the zeolite. Particularly, the presented evidence indicated that conventional impregnation favors a heterogeneous distribution of nickel over the zeolite while ion exchange favor the location of nickel inside its micropores.

Considering the above, this work revisits the properties and performance of monometallic nickel catalysts supported on various carriers; namely, SiO_2, γ-Al_2O_3, H^+-Y zeolite, and a microporous-mesoporous H^+-Y zeolite. It is well established that these carriers have different acidities; SiO_2 is considered neutral, γ-Al_2O_3 is a Lewis acid, while the zeolites have both Brönsted and Lewis acidity.[72,73] The synthesis of the catalysts was done by impregnation under conditions that favor the electrostatic interaction between the dissolved ionic nickel species and the surface electrostatic charges of the supports.[74,75] The loading of nickel was estimated after considering the impregnation of a statistical monolayer of the metal over the support less populated by surface hydroxyls. Catalysts were tested in the hydrodesulfurization of dibenzothiophene after in-situ reduction with H_2. The latter procedure was adopted assuming that metallic nickel moieties are active in hydrodesulfurization. The paper illustrates the rationale of the synthesis method and its correlation of the properties of the catalysts that are key to their performance in the tested reaction are discussed.

Results

Physicochemical properties of the catalysts

The physicochemical properties of the synthetized catalysts are discussed below and a comparison of these results with the ones obtained for the supports is presented in Table 1 and Table **2**.

Bulk Ni loading

The rationale for selecting the nominal loading of nickel in the catalysts was to make a theoretical monolayer of nickel over the support with the lowest surface area. Results indicated that this support was silica, SSA_{BET} = 15 ± 1 $m^2 \cdot g^{-1}$, Table 1. Calculations for attaining a theoretical monolayer of nickel over this SiO_2 thus yielded a nominal value of 0.5 wt.% of nickel. We kept this loading constant for all catalysts.

The values for the bulk Ni loading for each catalyst, obtained from the atomic absorption spectrometry, are presented in column 9 in Table 2. These results showed that the efficiency of the impregnation of nickel was almost complete since the final bulk loading of nickel in all catalysts (except for the Ni/SiO_2 catalyst) was very close to the theoretical loading used for the synthesis, i.e., 0.5 wt.%. In the case of Ni/SiO_2, the results found herein are similar to those reported by Mhadmhan *et al*.[76] They prepared a Ni catalyst supported on a low surface area silica-fiber (SF) by different impregnation methods. The catalyst prepared by the SEA method had about 80% of the theoretical Ni loading that they established, in contrast with the other catalysts where the Ni loading was 100%.

Specific surface area and porosity

The textural properties of the catalysts were analyzed after recording Ar physisorption isotherms on samples from the fresh supports and catalytic powders and from samples taken after the pelletizing procedure done for producing the particle size distribution required for the hydrodesulfurization reaction tests, see Catalytic Tests in Experimental Section. The recorded Ar physisorption isotherms are shown in Figures S4 and S14 of the Supporting Information (SI) where their features are discussed. In general, no evident changes in porosity were seen when comparing the catalysts with the supports; see Table 1 and pores size distributions in Figures S5, S6, and S15-S18. Therefore, it was assumed that nickel particles were homogeneously dispersed over the SiO_2, γ-Al_2O_3, and H^+-Y zeolite supports. A metric that supports this assumption is $NSSA_{BET}$,[77–79] Equation 2, whose values are shown in the last column in Table 1. Indeed, all $NSSA_{BET}$ values for these catalysts were higher or equal to 0.95. In the case of the catalysts supported on the mesoporous H^+-YM zeolite, $NSSA_{BET}$ values were below 0.90 which suggests a relative decrease in the dispersion of Ni. But comparatively, the SEA method led to better dispersed Ni particles over this support as compared to conventional wet impregnation: $NSSA_{BET}$= 0.87 for Ni/H^+-YM > $NSSA_{BET}$= 0.81 for Ni/H^+-YM(WI).

Analysis of the impregnation of Ni

To analyze the adsorption of Ni during the impregnation of the supports, we studied and compared the proton affinity distributions for both the supports and the catalysts. Figure 1 shows the proton affinity distribution curves for the catalysts compared with the supports. The recorded trends showed a high consumption of surface OH groups for all catalysts prepared by

Table 1. Summary of the textural properties of materials.

Sample	SSA_{BET} ($m^2 \cdot g^{-1}$)	SSA_{Micro} ($m^2 \cdot g^{-1}$)	SSA_{Meso} ($m^2 \cdot g^{-1}$)	PV_{NLDFT} ($cm^3 \cdot g^{-1}$)	PS_{NLDFT} (nm)	PS_{BJH} (nm)	C_{BET}	$NSSA_{BET}$‡
SiO_2	15 ± 1	--	15 ± 1	0.06 ± 0.00	--	12.72 ± 2.41	67 ± 17	--
Ni/SiO_2 (Pow.)	17 ± 2	--	17 ± 2	0.06 ± 0.00	--	12.72 ± 0.82	65 ± 6	0.95
Ni/SiO_2 (Cat.)	18 ± 1	--	18 ± 1	0.07 ± 0.02	--	11.85 ± 1.76	58 ± 13	
Al_2O_3	132 ± 12	--	132 ± 12	0.43 ± 0.01	--	10.70 ± 0.05	53 ± 15	--
Ni/Al_2O_3 (Pow.)	137 ± 8	--	137 ± 8	0.42 ± 0.01	--	10.59 ± 0.56	33 ± 6	0.97
Ni/Al_2O_3 (Cat.)	142 ± 22	--	142 ± 22	0.38 ± 0.03	--	9.53 ± 0.35	40 ± 12	
H^+-Y	810 ± 85	724 ± 89	86 ± 4	0.32 ± 0.03	0.74 ± 0.04	--	1873 ± 157	--
Ni/H^+-Y (Pow.)	801 ± 34	707 ± 47	94 ± 13	0.32 ± 0.01	0.73 ± 0.01	--	1997 ± 205	0.98
Ni/H^+-Y (Cat.)	650 ± 98	571 ± 72	79 ± 26	0.26 ± 0.04	0.72 ± 0.01	--	2025 ± 334	
H^+-YM	760 ± 85	497 ± 140	263 ± 55	0.41 ± 0.00	0.71 ± 0.01	2.54 ± 0.95	1151 ± 326	--
Ni/H^+-YM (Pow.)	662 ± 51	374 ± 88	288 ± 42	0.38 ± 0.00	0.69 ± 0.04	2.54 ± 0.87	1108 ± 96	0.87
Ni/H^+-YM (Cat.)	573 ± 38	319 ± 28	254 ± 48	0.33 ± 0.03	0.70 ± 0.03	2.72 ± 0.77	1095 ± 57	
Ni/H^+-YM(WI) (Pow.)	618	336	282	0.34	0.71	2.95	874	0.81
Ni/H^+-YM(WI) (Cat.)	562 ± 31	369 ± 63	193 ± 94	0.29 ± 0.05	0.71 ± 0.00	3.14 ± 0.11	1157 ± 355	

Cat. = Catalysts at 300-600 µm. Pow. = Catalyst Powders. ‡Measurements made with powders before tableting.

Table 2. Summary of the chemical properties of materials.

Sample	PZC	OH density ($OH \cdot nm^{-2}$)‡	OH conc. (mmol/g)‡	BAS conc. (µmol/g)‡	LAS conc. (µmol/g)‡	Total conc. of AS (µmol/g)‡	BAS/ LAS	Bulk Ni loading (wt.%)‡	Conc. of surface Ni (wt.%)‡	Conc. of surface Ni (At.%)‡
SiO_2	3.0 - 4.0	6.8	0.17	--	--	--	--	--	--	--
Ni/SiO_2 (Pow.)	NM	2.7	0.07	--	--	--	--	0.26	NM	NM
Ni/SiO_2 (Cat.)										
Al_2O_3	7.1	8.1	1.77	0	62	62	0	--	--	--
Ni/Al_2O_3 (Pow.)	NM	3.6	0.81	0	36	36	0	0.46	3.37	1.14
Ni/Al_2O_3 (Cat.)										
H^+-Y	3.9	1.0	1.34	352	91	444	4	--	--	--
Ni/H^+-Y (Pow.)	NM	0.9	1.25	347	69	417	5	0.46	1.39	0.46
Ni/H^+-Y (Cat.)										
H^+-YM	4.9	1.3	1.66	243	87	330	3	--	--	--
Ni/H^+-YM (Pow.)	NM	1.1	1.25	251	72	323	3	0.43	4.04	1.31
Ni/H^+-YM (Cat.)										
Ni/H^+-YM(WI) (Pow.)	NM	1.5	1.50	147	92	239	2	0.50	1.10	0.36
Ni/H^+-YM(WI) (Cat.)										

Cat. = Catalysts at 300-600 µm. Pow. = Catalyst Powders. ‡Measurements made with powders before tableting. NM: Not measured. Conc.: concentration. BAS: Brönsted Acid Sites. LAS: Lewis Acid Sites. AS: Acid Sites.

the SEA method, especially for those with the lower surface areas, i.e., silica and alumina. Indeed, the PAD curves of these materials were basically flat. Conversely, the PAD curves for the catalysts supported over the H^+-Y and the H^+-YM zeolites showed that a high number of surface hydroxyls were still free to adsorb nickel. In general, the ensemble of these results confirms that the SEA method has high selectivity for impregnating a metal over surface hydroxyls.[74,75,80,81] In contrast, the Ni/H^+-YM(WI) catalyst, which was prepared by the typical wet impregnation method, basically displayed the same PAD curve of the H^+-YM support which evidences the poor specificity of conventional impregnation. Further confirmation of the selectivity of the SEA method to deposit Ni over surface hydroxyls was found by analyzing the -OH region of Fourier Transform Infrared spectra recorded for both supports and catalysts (see Figure S22 in the SI).

Analysis of the acidity of the catalysts

Figure 2 shows the comparison of the pyridine adsorption spectra at 300 °C between the supports and the catalysts. Other pyridine adsorption FTIR spectra are shown in Figures S12 and S23 of the Supporting Information. The particulars of these results are: First, the impregnation of Ni over the SiO_2 support did not change the original acid nature of the support. Indeed, a complete overlap between the spectra for both SiO_2 and Ni/SiO_2 was found, Figure 2a. Moreover, it was necessary to multiply both spectra by a factor of 5 to amplify the signal and analyze the differences. Second and

similarly to results discussed above, both the Al_2O_3 support and the Ni/ Al_2O_3 catalyst showed the same pyridine adsorption spectra, but the impregnation of Ni led to a ca. 42% decrease in Lewis acidity (Figure 2b).

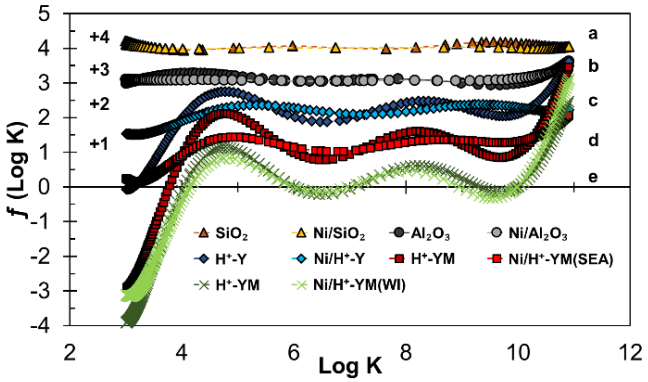

Figure 1. Comparison of Proton Affinity Distribution curves between supports and catalysts. (a) SiO_2 & Ni/SiO_2, (b) Al_2O_3 & Ni/ Al_2O_3, (c) H^+-Y & Ni/H^+-Y, (d) H^+-YM & Ni/H^+-YM, and (e) H^+-YM & Ni/H^+-YM(WI).

Third, for the catalysts supported on zeolites and synthesized the SEA method; namely, Ni/H^+-Y and Ni/H^+-YM, kept their most of their Brönsted acidity (bands at 1545 cm^{-1} in Figure 2c and 2d and column 5 in Table 2). In contrast, the Lewis acidity (bands at 1455 cm^{-1} in Figure 2c and Figure **2**d and column 6 in Table 2) decreased by around 20% (see column 6 in Table 2). This latter result agrees with previous studied made by Kang *et al*.[82–84]. At this point, the differences between the SEA method and conventional wet impregnation were evident since the latter led to a loss of around 40% in the original Brönsted acidity of the H^+-YM support as compared to Ni/H^+-YM(WI) catalyst, Figure 2d and Table 2. Meanwhile, the Lewis acidity of the Ni/H^+-YM(WI) catalyst was rather similar to the Lewis acidity of the H^+-YM support. The results found for the Ni/H^+-YM(WI) catalyst are in agreement with the literature regarding the impregnation of zeolites via regular impregnation.[85]

Surface chemical state of Ni

The surface chemical state of nickel in the catalysts was assessed by XPS, except for Ni/SiO_2 which was not measured. XPS results showed the following. First, nickel was best dispersed over the H^+-YM support when the SEA method was used. Particularly, the Ni/H^+-YM catalyst had the highest concentration of surface Ni among all materials (columns 10 and 11 in Table 2). Indeed, this value was thrice bigger than the concentration of surface Ni for the catalyst synthesized by the wet impregnation method – Ni/H^+-YM(WI) – and for the Ni/H^+-Y catalyst. Second, in all spectra, Figure 3, Ni was found to be in an oxidized state since the position of the Ni $2p_{3/2}$ core level was positively shifted with respect to metallic Ni (at 852.8 eV from NIST database[86]). For the Ni/Al_2O_3 catalyst, the position for the Ni $2p_{3/2}$ peak was ~856.0 eV, which is close to $Ni(OH)_2$ species (856.3 eV). This suggested that $NiAl_2O_4$ species did not form since the latter appears around 857.2 eV.[87] In the case of the catalysts Ni/H^+-Y and Ni/H^+-YM, Figure 3a, nickel was found around 857.1 and 857.0 eV, respectively, which suggests that both zeolite-based catalysts presented $NiAl_2O_4$ species on their surface.[88] On the other hand, since nickel was not detected by XPS for the Ni/H^+-YM(WI) catalyst, Figure 3a, we made XPS measurements for Ni/H^+-YM and Ni/H^+-YM(WI) using a polychromatic Al Kα radiation which produces more intense signals. Additionally, we compared the spectra for the samples from these two catalysts after in-situ reduction at 400 °C using 100 mL · min^{-1} of H_2 flow for 4 h. The purpose was examining the chemical state of the catalysts at the beginning of the catalytic tests. Figure 3b shows the Ni 2p spectra for Ni/H^+-YM and Ni/H^+-YM(WI) using the polychromatic Al Kα radiation. On the one hand, the results for the Ni/H^+-YM catalyst showed that nickel was partially reduced to $Ni(OH)_2$, Ni $2p_{3/2}$ signal at ~856.5 eV, after the H_2 treatment. However, the reduction degree of Ni in Ni/H^+-YM was lower than the one showed by the metal in the Ni/H^+-YM(WI) catalyst since for the

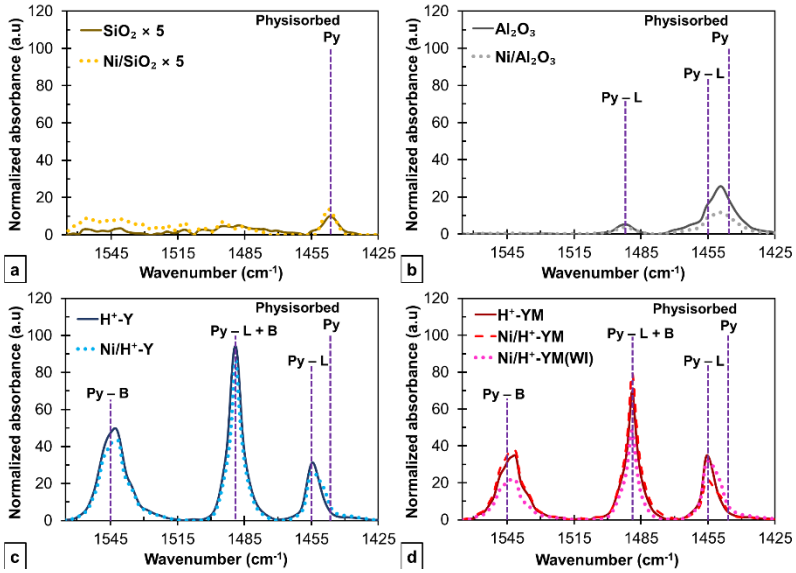

Figure 2. Comparison of FTIR spectra for pyridine adsorption at 300 °C between supports and catalyst for: (a) SiO_2 & Ni/SiO_2, both multiply by factor of 5 (b) Al_2O_3 & Ni/Al_2O_3, (c) H^+-Y & Ni/H^+-Y, (d) H^+-YM, Ni/H^+-YM, & Ni/H^+-YM(WI). The band at 1545 cm^{-1} corresponds to pyridine adsorption on Brönsted acid sites (Py – B). The band at 1445 cm^{-1} corresponds to pyridine adsorption on Lewis acid sites (Py – L). The band at 1490 cm^{-1} corresponds to an overlap of the signals from pyridine adsorbed on both the Brönsted and the Lewis sites (Py – L + B), and the band at 1445 cm^{-1} corresponds to physically adsorbed pyridine.[89–91]

latter the Ni $2p_{3/2}$ signal was found at ~855.7 eV. These findings agree with previous studies showing that metallic nanoparticles (Pd, Pt, etc [6,92]) over zeolites are hard to reduce. For example, Long-Xiang *et al*.[88] impregnated Ni onto USY zeolites using nickel naphthenate dissolved in benzene and found that Ni remained in an oxidized state after H_2 reduction at 500°C and also after steaming. The authors ascribed this tendency to the strong tendency of Ni to bind to the aluminum moieties of the zeolite.

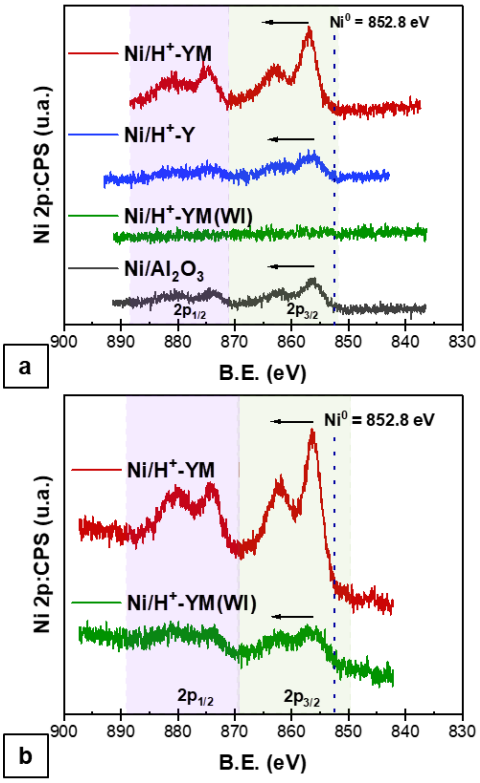

Figure 3. XPS spectra for Ni 2p for Ni/Al_2O_3, Ni/H^+-Y, Ni/H^+-YM, and Ni/H^+-YM(WI) using a radiation of: (a) monochromatic Al Kα and (b) polychromatic Al Kα.

Catalytic performance in the hydrodesulfurization of dibenzothiophene

First, we discuss the evolution of the catalytic performance with time on stream and second, we address the distribution of reaction products over the tested catalysts.

Evolution of dibenzothiophene conversion with time on stream

Figure 4 shows the evolution of dibenzothiophene conversion with time on stream for the synthesized catalysts. Results show that all catalysts and even the H^+-YM (tested as reference) converted dibenzothiophene during the first hour of the reaction. Among the catalysts, Ni/H^+-YM showed the highest conversion and Ni/Al_2O_3 the lowest. These results corroborate that monometallic nickel catalysts are active in the hydrodesulfurization.[57,63,64,66,70,71] The novelty of our work is that we particularly show that dispersed nickel is active in the hydrodesulfurization of the more refractory dibenzothiophene under typical reaction conditions. In this sense, the most recent report by Zhao *et al*.[57] showed that a Ni/Al_2O_3 hydrodesulfurized thiophene; a molecule way more reactive than dibenzothiophene, at a much higher temperature, 370 °C, than the one used herein.

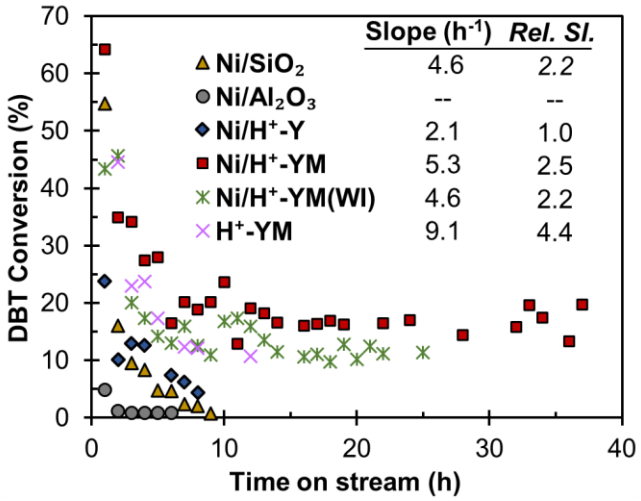

Figure 4. Activity versus time on stream for the catalysts: Ni/Al_2O_3, Ni/SiO_2, Ni/H^+-Y, Ni/H^+-YM, and Ni/H^+-YM(WI) and the H^+-YM support. Slope calculated with data until 10 h. *Rel. Sl.:* relative slope from the Ni/H^+-Y slope.

The initial activity of the catalysts was followed by deactivation during the next 6 h of time on stream (Figure 4), except for Ni/Al_2O_3 which was almost completely deactivated after two hours. The observed tendencies showed that nickel plays a role in slowing the deactivation of the catalysts. In this sense, we estimated an apparent rate of deactivation (h^{-1}) for the catalysts from the absolute value of the slope of the conversion data between 1-6 or 10 h, inset in Figure 4. After noticing that Ni/H^+-Y had the lowest apparent deactivation rate among the tested catalyst, we decided to use the apparent deactivation rate for Ni/H^+-Y as a reference for estimating relative deactivation values. Henceforward, we noticed that the H^+-YM zeolite was deactivated 4.4 times faster than the Ni/H^+-Y catalyst. In addition, the deactivation of H^+-YM was approximately twice as fast as compared to the deactivation of Ni/H^+-YM and Ni/H^+-YM(WI). Furthermore, after the initial period of deactivation, the Ni/H^+-YM and Ni/H^+-YM(WI) catalysts showed an apparent stabilization during the rest of the catalytic tests. In the case of Ni/H^+-YM, its behavior was stable up to 40 h of time on stream.

Overall, Figure 4 and Figure 5 show that Ni/H^+-YM was the most active catalyst. This material had the highest concentration of surface Ni, Table S6, plus a well-developed micro-mesoporous structure with an acidity that was similar to the parent H^+-Y zeolite (Table 1 and Table 2). Comparing the conversion of dibenzothiophene over Ni/H^+-YM and over the wet impregnated Ni/H^+-YM(WI) catalyst, the former converted ca. 45% more dibenzothiophene than the latter at the apparent steady state of the reaction, Figure 5. These differences in catalytic performance can be correlated to the fact that the SEA method disperses Ni much better than conventional impregnation. Indeed, the surface concentration of Ni in the Ni/H^+-YM catalyst was more than thrice the one found for the wet impregnated Ni/H^+-YM(WI) catalyst. Results also showed the advantages of introducing mesoporosity in the zeolites while keeping the acidity unaltered. Similar results concerning the introduction of mesopores for a H^+-Y zeolites used

as supports for Pd based catalysts were found by Fu *et al*.[93] who showed how the activity in the hydrodesulfurization of dibenzothiophene of Pd/mesoporous H^+-Y was boosted.

Analysis of the distribution of reaction products

Figure 5 shows the average distribution of reaction products for each tested material at conditions of apparent steady state of dibenzothiophene conversion (values marked with a star in the plot). The main reaction products were tetrahydro-DBT (THDBT), biphenyl (BP), and cyclohexylbenzene (CHB). In the case of the zeolite-based catalysts, the recorded chromatograms showed the production of compounds that are heavier than DBT. They were assumed to be alkylated DBTs, accordingly. In addition, an important fraction of lighter products was found but could only be partially identified. These products are presented as "Other products" in Figure 5.

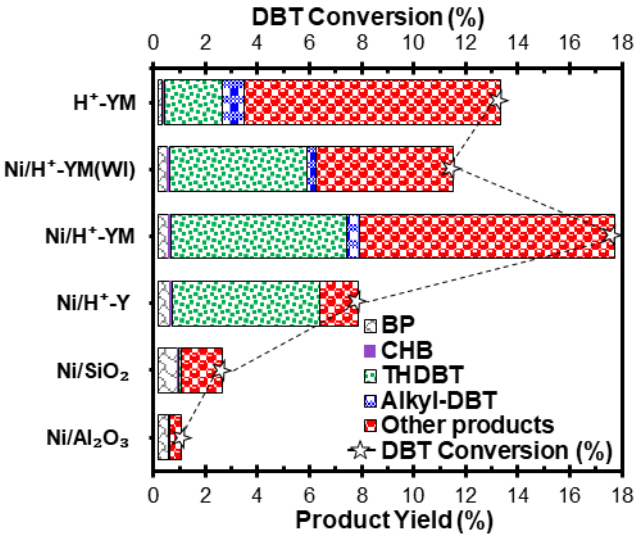

Figure 5. Distribution of reaction products (yields) as a function of the average conversion of dibenzothiophene at apparent steady state for the catalysts: Ni/Al_2O_3, Ni/SiO_2, Ni/H^+-Y, Ni/H^+-YM, and Ni/H^+-YM(WI), and the H^+-YM support.

Considering the ensemble of reaction products, we propose the reaction scheme presented in Figure 6. According to results, the catalysts supported on SiO_2 and Al_2O_3 were mainly selective to the direct route of desulfurization (Figure 5 and purple box delimited by a dashed line in Figure 6). In contrast, the catalysts supported on the zeolites displayed a higher selectivity to the hydrogenation mediated route of hydrodesulfurization (Figure 5 and pink zone delimited by a dotted line in Figure 6). This clearly shows an influence of the acidic characteristics of the supports on the selectivity of the reaction. Namely, Al_2O_3, that is provided only with Lewis acid sites promoted the direct desulfurization pathway, while the zeolites promoted cracking and alkylation reactions owing to Brönsted acid sites.[94–96] In this sense, we recall that the mesoporous H^+-YM zeolite was active in the reaction by itself, Figure 4 and Figure **5**. Particularly, the mesoporous H^+-YM zeolite catalyzed partial hydrogenation, cracking and alkylation reactions. The introduction of nickel enhanced the catalytic performance mostly by promoting hydrogenation and by allowing C-S scission either via hydrogenation mediated or direct desulfurization, Figure 5.

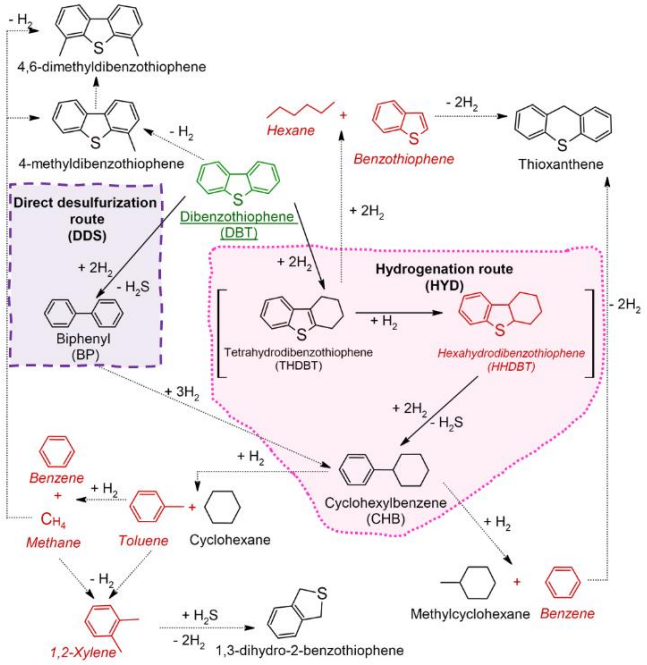

Figure 6. Reaction scheme proposed for hydrodesulfurization of dibenzothiophene when using Ni/H^+-YM type catalysts owing GC-MS results. Products previously reported in the literature[24,26] are shown in red (*italic*) font although we did not found them in the GC-MS analysis.

Discussion

On the properties of the catalysts synthesized with the strong electrostatic adsorption method

The results of the physicochemical characterization of the materials demonstrated a better and stronger metal-support interaction via strong electrostatic adsorption compared with the conventional impregnation method. Although we did not directly measure the metal-support interaction, we took it that it can be assessed indirectly from the trends that we found during the characterization of the materials. Namely, we assumed that stronger metal-support interactions are reflected by better a dispersion of nickel and by controlled effects on the surface chemical state of nickel and on the acidity of the catalysts.

As commented in the results section, we found evidence of a uniform and high Ni dispersion over the supports. The evidence can be summarized as slight or negligible changes in the textural properties of the materials and as controlled changes in the acid properties of the catalysts. However, we were not able to directly measure dispersion due to the limitations of our characterization techniques at the low loadings that we used. Nevertheless, it must be said that high metallic dispersion is considered a distinctive trait of the strong electrostatic adsorption impregnation method.[76,82–84,91,97,98]

As discussed in the results section, we found evidence of the formation of $NiAl_2O_4$ species in the zeolite supported nickel catalysts synthesized with the SEA method. On the one hand, this species contributed to the Lewis acidity of these catalysts

although the total concentration of Lewis acid sites of the materials decreased slightly as compared to the zeolite supports. Such a result agrees with the absence of NiO particles that are known to reduce the Lewis acidity of zeolite supports when they form.[88,90,91,97–100] Furthermore, the XPS analysis of in-situ reduced Ni/H$^+$-YM showed that $NiAl_2O_4$ was partially reduced to $Ni(OH)_2$. This result suggests that the formed $NiAl_2O_4$ species are indeed highly dispersed over the H$^+$-YM zeolite since it is known that large crystalline $NiAl_2O_4$ particles are basically irreducible under the temperature conditions used herein.[101–103] Crystalline $NiAl_2O_4$ particles are typically formed when nickel is impregnated by conventional methods on Al_2O_3.[100,103] One of the merits of the SEA method is that these species are not formed on Ni/Al_2O_3 catalysts. Indeed, our results (XPS and FTIR analysis of adsorbed pyridine) showed that $NiAl_2O_4$ did not form in the Ni/Al_2O_3 catalyst. Instead, nickel was found to be present as NiO in the Ni/Al_2O_3 catalyst at the expense of Lewis acid sites, Table 2. On the other hand, we found that the Brönsted acidity of the zeolite supported catalysts synthesized with the SEA method remained basically the same after nickel impregnation (Table 2, and Figure 1 and Figure **2**). Therefore, we ascertain that the SEA method selectively targeted Lewis acid sites linked to the aluminium moieties of the zeolites and led to the formation of highly dispersed $NiAl_2O_4$ that are reducible Lewis acid sites. The latter was in contrast to what happens when conventional impregnation was done; as we discussed for the Ni/H$^+$-YM(WI) catalyst and as from the multiple results found in the literature.[6,87,88,92] Herein, we presented further evidence that conventional wet impregnation of Ni over H$^+$-YM leads to non-selective deposition over the hydroxyls of the zeolite. See proton affinity distribution curves (Figure 1), pyridine-TPD results (Figure 2), and the -OH region of Fourier Transform Infrared spectra (Figure S22 in the SI) for this catalyst. These trends correlated well with both a lower dispersion of Ni and a reduction in the Brönsted acidity of Ni/H$^+$-YM(WI). The latter has also been observed by other authors.[90,91,102]

Analysis of the stability of the catalysts

As we mentioned in the results section, after an initial period of deactivation, the samples from the H$^+$-YM zeolite, Ni/H$^+$-YM, and Ni/H$^+$-YM(WI) catalysts showed an apparent stabilization during the catalytic tests. This contrasted with what we found for the Ni/SiO_2 and Ni/Al_2O_3 catalysts. In this sense, Ni/SiO_2 showed a high initial conversion of dibenzothiophene, but it was deactivated too quickly, nonetheless. The literature ascribes this to the adsorption of H_2S[104] which in turn leads to the formation of a stable nickel sulfide phase[105,106] that is unable to regenerate the active sites of the catalyst. Catalyst regeneration is a necessary step in a catalytic cycle, which is observed in materials with different kinds of acidities and evaluated under hydrotreating reactions.[107] Since Ni/SiO_2 does not have the capability to regenerate itself, its main use for sulfur elimination from fuels is as an adsorbent.[108–112] Similar to Ni/SiO_2, Ni/Al_2O_3 showed a very poor performance. Rapid deactivation of Ni/Al_2O_3 due to the formation of nickel sulfide has been reported earlier.[113] The difference between SiO_2 and Al_2O_3 is that the latter is able to chemisorb H_2S,[114–116] hence aggravating the problem of active site regeneration.[107]

Some authors reported that coke formation also plays an important role in the deactivation of alumina-supported catalysts.[117,118] In this sense, for the zeolite supported catalysts and the H$^+$-YM support, we found a positive linear correlation between the apparent pseudo-first order kinetic constants for the production of alkyl-dibenzothiophenes and other products (Figure 7) and the absolute values of the apparent deactivation rate of these catalysts. Namely, an increase in the formation of these products implied a higher deactivation rate. Extensive literature shows that this result is related to the formation of coke on the active sites of the catalyst.[119–121] Herein, the following arguments can be given for considering the role of coke formation on the performance of the synthesized catalysts. (i) We found a strong correlation between the Lewis acid sites and the formation of "Other products" which are most probably cracking products (see Figure S38 in the SI). This result is in contrast with the commonly reported trends where the cracking reactions are attributed to the Brönsted acid sites.[101,122–124] (ii) We also noticed a correlation between the concentration of accessible Brönsted acid sites for the zeolite-based catalysts and the formation of alkyl-dibenzothiophenes (see Figure S41 in the SI). This tendency agrees with the literature.[125] And, (iii) due to the known proximity between Brönsted and Lewis acid sites, there is a high probability that the radicals, carbocations, produced on the Lewis acid sites can react with dibenzothiophene chemisorbed either on Brönsted acid sites or on Ni sites near the latter. The literature shows that carbocations strongly adsorb, block, and deactivate the acid sites of the zeolites.[119–122]

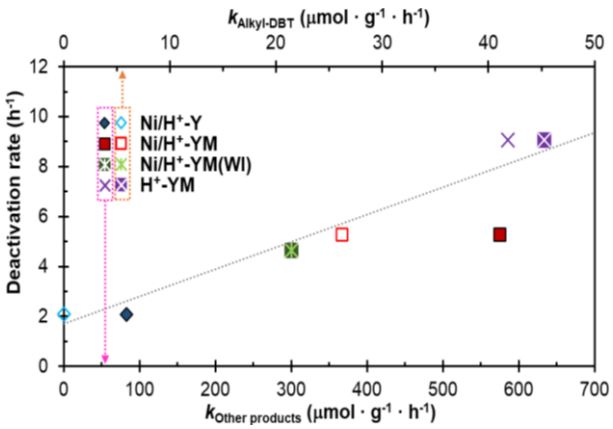

Figure 7. Correlation between the formation of alkyl-DBTs and "Other products" and the deactivation rate of the materials based on zeolites evaluated.

Catalytic functionalities of the materials

According to the literature, the role of the metal is key to the stability of the catalysts because its hydrogenation functionality facilitates the regeneration of the active phases by promoting the hydrogenation of adsorbed carbocation type species that interrupts the coking of the catalytic surface.[107] Our results suggest that the metal-support interaction generates an apparent stability in zeolite supported catalysts. Comparing the catalytic performance of the Ni/zeolite catalysts with the H$^+$-YM support, the formation of tetrahydrodibenzothiophene, cyclohexylbenzene, and biphenyl was always higher for the former, Figure 5. Thus, the interaction of nickel with the acid sites of the catalysts leads to developing the hydrogenation route of desulfurization and to C-S bond scission. Similar trends have been reported earlier in the literature.[101,122–124,126–128] Herein, we emphasize that the zeolite supported Ni catalysts mainly produced

tetrahydrodibenzothiophene which confirms the hydrogenating character of this metal under hydrotreatment reaction conditions.[129] Therefore, supported Ni catalysts are clearly bifunctional as other zeolite based metallic catalysts are.[101,122–124,126–128] In this sense, Figure 8 shows positive correlations between the conversion of dibenzothiophene and the apparent rates of formation of tethrahydrodibenzothiophene, cyclohexylbenzene, and biphenyl, and the density of the Brönsted acid sites of the catalysts. This trend is interesting because it reinforces our previous discussion on the role that Lewis and Brönsted acid sites play during the hydrodesulfurization reaction. Namely, the Lewis acid sites of the zeolites promote the formation of carbocation type species that lead to cracking and isomerization reactions while Brönsted acid sites promote hydrogenation in conjunction with nickel moieties which keeps the metal active during C-S scission.

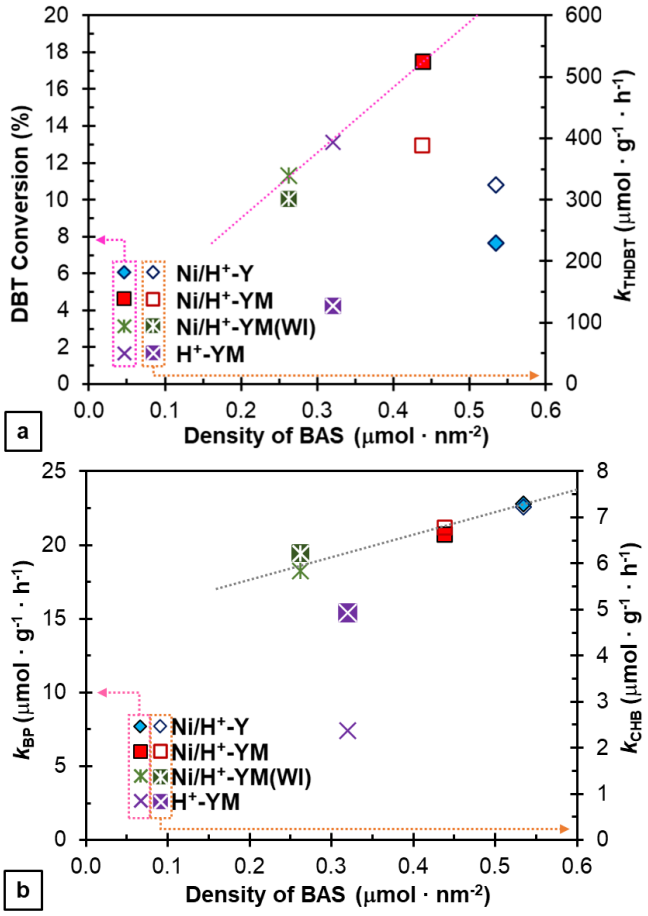

Figure 8. (a) Correlation between the DBT conversion and the formation of tetrahydrodibenzothiophene and the density of BAS. (b) Correlation between the formation of biphenyl and cyclohexylbenzene and the density of BAS.

Role of active sites accessibility

There were clear differences between the properties of the materials provided with mesopores and the Ni/H$^+$-Y catalyst, which is only provided with micropores, Figures S4 and S14, and Table 1 and Table **2**. We particularly notice that when correlating the Brönsted acidity of the catalysts with the catalytic performance, all mesoporous materials showed straightforward correlations between conversion of dibenzothiophene, the density of Brönsted acid sites, Figure 8a, and the density of surface hydroxyl groups, Figure 9, while the results for the Ni/H$^+$-Y catalyst appeared as outlier within these plots. Adding mesoporosity to zeolites enhances the accessibility to its acid sites hence improving the performance of metal based catalysts in hydrotreating reactions.[93,121] Herein, we also show that if the impregnation of the metal is made with the strong electrostatic adsorption method, the functionalities of the metal during the hydrotreating reactions (see Figure 8a where the apparent reaction rate constant for tetrahydrodibenzothiophene was always higher for the zeolite based catalysts synthesized with the SEA method as compared) are enhanced due to its deposition over specific surface hydroxyls and higher dispersion of partially reducible $NiAl_2O_4$ species.

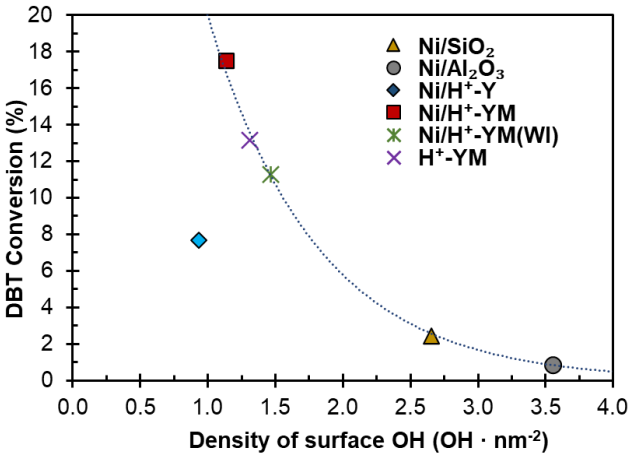

Figure 9. Conversion of dibenzothiophene in function of the density of surface hydroxyls and the density of the Brönster acid sites.

Conclusions

Ni particles were impregnated on four materials with different acid characteristics using the principles of strong electrostatic adsorption, which were evaluated in the hydrodesulfurization of dibenzothiophene. This work presented a synthesis method of catalysts based on the electrostatic interaction between the metallic phase and the support, and the correlation of the materials properties that are key to their performance in the tested reaction. The results showed that Ni nanoparticles are catalytically active in the hydrodesulfurization of DBT and that zeolites provide them with long-term stability. In addition, providing mesoporosity to the zeolite improved the catalytic performance. Likewise, using SEA impregnation was essential to obtain catalysts with high Ni dispersion, promoting a higher catalytic activity, which was caused by the strong interaction between Ni and the Brönsted and Lewis acid sites. Overall, we demonstrate that Ni particles may behave in the same manner as noble metals such as Pt, Pd, and Ir behave in hydrodesulfurization.

Experimental Section

Catalytic supports. The following materials were used to obtain the catalytic supports: sodium loaded silica (Na-SiO_2, Commercial Grade), extruded alumina (Al_2O_3, Sasol), and a Na-Y zeolite powder with nominal molar ratio Si/Al ~ 2.6 (Aldrich).

Pretreatment of the SiO_2 and Al_2O_3 supports. The sodium loaded SiO_2 was washed for 24 h by the reflux method,[130] in order to remove sodium. For this, a flat-bottomed flask containing a mixture of SiO_2 and hydrochloric acid (HCl, Merck, 37% fuming) solution at 1 M in a ratio of 100 g of SiO_2 · L^{-1} of the acid solution was placed in a sand bath heated at 68 °C. The mouth of the flask was connected to a Friedrichs condenser. The SiO_2/HCl mixture was stirred at 100 rpm with a magnetic stirrer. After washing, the recovered silica particles were filtered using filter paper (*Grade: 392*, BOECO) and thoroughly washed with deionized water (0.055 μS · cm^{-1}) until a neutral pH was reached. Finally, the sodium free silica was dried at 80 °C for 18 h in a static oven (*Precision Premium Mechanical Convection - PR305045M*, Thermo Scientific). The removal of Na from the material was confirmed by X-ray photoelectron spectroscopy (XPS), see Supporting Information Appendix A, Figure S1.

On the other hand, the extrudates of alumina were crushed with mortar and pestle and then sieved to a particle size between 25-75 μm (mesh numbers:500 and 200, respectively, and sieve diameter: ~13 cm). This particle size was the same as for the other catalytic supports.

Mesopores generation in Na-Y zeolite and further ionic exchange. A micro-mesoporous Na-Y zeolite was synthesized by adapting the surfactant-templating method of García-Martínez.[131] The zeolite was dispersed in deionized water with a ratio of 1 g of zeolite to 4 mL of water. Then, a 0.167 M solution of citric acid ($C_6H_8O_7$, Merck, 99%) was added dropwise to the suspension. Under such conditions, a zeolite/solution ratio of 100 g Na-Y · L^{-1} was obtained. The suspension was maintained under constant stirring at 200 rpm for 1 h. The zeolite was recovered and washed with deionized water until a neutral pH was reached. The recovered powder was further dried for 2 h at 60 °C and then dispersed in an aqueous solution of 0.22 M of hexadecyltrimethylammonium bromide (CTAB, Sigma-Aldrich, 98%) and 0.025 M of NaOH (Merck, 99%) to obtain a zeolite/total solution ratio of 43 g of Na-Y · L^{-1} of solution. The suspension was stirred at 350 rpm for 20 min. Afterward, the produced slurry was transferred to a *Teflon-Lined Stainless-Steel Autoclave* reactor and put in an oven at 150 °C for 15 h. After removing the reactor from the oven and allowing its cooling for 15 min, the material was recovered by centrifugation in an *LC-04R* (Zenithlab) apparatus and washed with a methanol (Merck, 99%)-water (deionized) solution. The recovered solid was dried at 60 °C for 2 h. Finally, the recovered zeolite was calcined at 550 °C with a ramp of 1.5 °C · min^{-1} using a *CWF 1200* (Carbolite) furnace. This zeolite was called Na-YM.

Both the Na-Y and the Na-YM zeolites were transformed into their acid forms by ion exchange[132] with an ammonium nitrate solution (NH_4NO_3, PanReac AppliChem, 99%) at 0.1 M. For this purpose, a zeolite/solution ratio of 10 g · L^{-1} suspension was made and stirred at 300 rpm at room temperature for 8 h. Finally, the exchanged zeolites were filtered and allowed to dry at 60 °C overnight. The ion exchange was repeated thrice. After the third exchange, the zeolites were calcined at 550 °C for 6 h with a ramp of 2 °C · min^{-1}. The thus pretreated zeolites were called H^+-Y and H^+-YM.

Characterization of the Supports

Determination of the point of zero charge (PZC). PZC is defined as the condition at which the average surface charge density of an oxide equals zero.[133,134] This property was determined by the immersion technique;[135] also known as the drift method.[136] For the method, a 0.01 M solution of sodium chloride (NaCl, Merck, 99.5%) was prepared and divided equally into six beakers. Then, using 0.01 M NaOH or HCl solutions, the pH was adjusted to obtain values between 2 and 12. pH was read using a *HI 5522* (Hanna Instruments) pH meter, and the initial value recorded for the experiments was called $pH_{initial}$. Next, adequate amounts of each solid were added to the solution to sequentially make 3 mg sample · mL^{-1} of solution. These suspensions were stirred at 200 rpm at room temperature for 24 h. The pH recorded after these treatments were called pH_{final}. With these data, a curve of $\Delta pH\ vs\ pH_{initial}$ was plotted, where $\Delta pH = pH_{final} - pH_{initial}$, and finally, the $PZC \equiv pH_{PZC}$ was determined as the pH at which the curve intersects the abscissa axis, i.e., when $\Delta pH = 0$.

Table 2 presents the values of pH where the PZC for each one of the catalytic supports, see intersects with the abscissa axis in Figure S3 from Appendix B in the SI. With this information, it was possible to establish the impregnation pH at basic values and the use of nickel nitrate hexahydrate ($Ni(NO_3)_2$×$6H_2O$, Merck, 99%) as precursor salt to do the impregnation by the SEA method.

Determination of the surface area and porosity of the materials. These properties were calculated with data from argon adsorption-desorption isotherms measured at -186.15 °C. Samples were weighed in 9 mm diameter cells made of borosilicate glass. Samples of ca. 0.1000 g were used for the zeolites, whereas ca. 0.1500 g were used for both the Al_2O_3 and the SiO_2 supports. Isotherms were measured in a *3FLEX™* (Micrometrics) apparatus in a relative pressure (P/P_0) range between $1.0×10^{-4}$ and 0.993 using 10 s equilibrium intervals. Before each analysis, powders were degassed for 2 h at 120 °C and then for 6 h at 300 °C to remove any type of impurities adsorbed on their surface. At the end of the degasification process, a vacuum pressure about 5 Pa was reached. This procedure was performed with a *Vac Prep 061* (Micrometrics) device. The complete procedure for the argon physisorption tests was replicated either twice or thrice for each material – except for the Ni/H^+-YM(WI) catalyst – in order to obtain an average value of the specific surface area and its corresponding standard deviation.

The surface area of the materials was assessed by the Brunauer-Emmet-Teller (BET) method,[137] after doing an optimization of the C_{BET} constant following the Rouquerol *et al*. consistency criteria.[138] The contribution of microporosity to the surface area of the materials was assessed with the t-plot method.[139] For t-plot calculations, we applied the Harkins and Jura reference isotherm. We selected the data from a region of the V_{ads} vs. *thickness* plot over which the linear fitting was above the data recorded in the P/P_0 region below ~0.4. The fitting procedure also considered selecting data where $R^2 \geq 0.999$.[140,141] The micropore size distributions were estimated by the Non-Local Density Functional Theory (NLDFT) using the Ar@87-Zeolites, H-form, method.[142] The mesopore size distributions were estimated with the Barret-Joyner-Halenda (BJH) method[143] using the Harkins and Jura standard isotherm[141] with the Faas correction to the Kelvin equation.[144] All the above calculations were done with the MicroActive® software provided with the *3FLEX™* apparatus.

Table 1 shows the values for the BET specific surface area (SSA_{BET}), micropore specific surface area (SSA_{Micro}), mesopore specific surface area (SSA_{Meso}), the calculated pore volumes (PV_{NLDFT}), and average pore sizes (PS_{NLDFT} and PS_{BHJ}). The corresponding

physisorption curves, cumulative pore volume curves, and pore size distribution curves for the supports, as well as their respective analysis, can be viewed in detail in the Appendix C in the SI. Table 1 shows that the specific area for SiO_2 was the lowest among the supports, followed by Al_2O_3, H^+-YM, and H^+-Y. We noticed that the mesoporous surface of the H^+-YM zeolite formed at the expense of the internal micropore specific area without destroying the zeolitic framework as evidenced by the fact that the average pore size of the micropores for both H^+-Y and H^+-YM is the same. Meanwhile, the formed mesopores in H^+-YM were almost one order of magnitude larger than the micropores.

Determination of the distribution of surface hydroxyls. Proton Affinity Distributions (PADs) were calculated for assessing the relative concentration of the surface hydroxyl groups of the supports.[145] Measurements were made by potentiometric titration with a *pH Module 867* (Metrohm). For the tests, ca. 0.1000 g of the samples were added to 30 mL of a 0.1 N aqueous solution of sodium nitrate ($NaNO_3$, Merck, 99.5%). The obtained suspension was homogenized by magnetic stirring for 60 min. For titration in the pH basic range, a 0.05 N aqueous solution of NaOH was used as titrating agent. Titration was made by automatically dosing 0.05 mL of the NaOH solution each 20-90 s until a pH of 10.9 was reached. Likewise, titration was performed in the acidic range for a fresh sample of the tested material with a 0.037 N nitric acid (HNO_3, Merck, 65% v/v) aqueous solution until a pH of 3.0 was reached. The changes in pH were measured in terms of the volume (basic or acidic) of the solution added. The acquired data were used to construct a proton consumption function $f(Log\,K)$ as a function of pH by a proton balance.[79,80,146,147]

Values for the OH surface density of the catalytic supports are presented in Table 2. Of course, SiO_2 had a lower concentration of surface hydroxyls as compared to the other materials. But, owing to its lowest surface area, the surface density of its hydroxyls was high; almost the same as the one Al_2O_3. Both SiO_2 and Al_2O_3 indeed showed the highest OH surface densities. As for the zeolites, the mesoporous structured H^+-YM displayed a slightly higher surface density of OH. PAD curves for each material are provided in Appendix D in the SI. We used this information to calculate the loading of nickel that makes a statistical monolayer over the support with the lowest surface area, i.e., SiO_2 (see the equations to perform the calculations in Appendix G in the SI). Therefore, it can be deduced that all the other catalysts had less than a monolayer of coverage of nickel while keeping the same metallic loading.

Determination of surface acid sites. The acidity of the materials was evaluated by the Fourier Transform Infrared Spectroscopy (FTIR) analysis of the adsorption of pyridine (C_5H_5N, J.T. Baker, 99.9%).[89] For each experiment, samples were pressed into self-supporting thin wafers, using 2 metric tons of pressure for 1 min (*Manual Press*, Specac). Pellets of 12.7 mm diameter and ~10.0 mg were obtained. The pellets were transferred to a cell equipped with ZnSe windows and a vacuum system (*Pfeiffer Hicube Eco Turbo*), that reaches a vacuum pressure of 1×10^{-4} Pa. Samples were outgassed at 450 °C and 1.5 °C · min^{-1} for 8 h to desorb water and other contaminants before adsorbing pyridine. Adsorption was carried out at 150 °C for 30 min followed by desorption at 25 °C, 150 °C, and 300 °C. For FTIR measurements, 128 scans from 400 cm^{-1} to 4000 cm^{-1} with a resolution of 4 cm^{-1}, and a spacing of 0.482 cm^{-1} were used in a *Nicolet iS50* (Thermo Scientific) apparatus. All absorbance results were normalized in regards of the pellet weight. The relative concentration of either Brönsted or Lewis acid sites was estimated using the following equation:

$$[BAS/LAS] = IA(BAS/LAS) \times \pi \times \frac{R^2}{W \times \varepsilon_{BAS/LAS}} \qquad (1)$$

Where, $[BAS/LAS]$ is the concentration of either the Brönsted or Lewis acid sites (μmol · g^{-1}), $IA(BAS/LAS)$ is the integrated absorbance of the selected Brönsted or Lewis band (cm^{-1}), R^2 is the radius of the sample wafer (cm), W is the weight of the wafer (g), and $\varepsilon_{BAS/LAS}$ is the molar extinction coefficient for the Brönsted or Lewis acid sites (cm · μmol^{-1}). For calculations, we used the values $\varepsilon_{BAS} = 1.59 \pm 0.62$ and $\varepsilon_{LAS} = 1.73 \pm 0.97$ for the zeolite-based materials and $\varepsilon_{LAS} = 1.37 \pm 0.37$ for the Al_2O_3-based materials. These values correspond to a t-Student 95% confidence interval for the media of the extinction coefficients reported in the literature.[148–158]

Impregnation of Ni. Catalysts were synthesized by adapting the Strong Electrostatic Adsorption method.[75,159] This method is based on the fact that when an oxide is suspended in an aqueous solution, its surface acquires either a negative or positive net charge as a function of the pH in relation to the PZC of the oxide. Namely, when the pH of the impregnating solution is above the PZC of the oxide, its surface hydroxyl groups protonate and become positively charged hence favoring the adsorption of anionic metal complexes from the impregnating solution. Conversely, if the pH is above the PZC, the hydroxyl groups from the oxide de-protonate, and the surface of the oxide becomes negatively charged hence promoting the selective adsorption of cations from the impregnating solution (see Figure 10a).[74]

For applying the method, one also needs to consider that the maximum density for an adsorbed ion complex with a *2+* charge corresponds to a close-packed monolayer of complexes that retain one hydration sheath, which corresponds to the surface hydroxyls density, as depicted in Figure 10b for the particular case of nickel impregnation.

The impregnation of Ni over the selected supports was carried out following the flowchart presented in Figure 11, which is explained as follows. First, we calculated the adequate loading of nickel aiming to achieve a statistical monolayer of the metal over the silica support, i.e., the support with the lowest surface area, see the SI for details. Accordingly, we calculated the corresponding weight of the nickel precursor: nickel nitrate hexahydrate ($Ni(NO_3)_2\times6H_2O$, Merck, 99%) and dissolve it in deionized water. The volume of this solution was obtained by considering a ratio of 1 g of support per 10 mL of solution.

Then, the necessary stoichiometric amount of an ammoniacal solution (NH_4OH, Merck, 25-30% v/v), see Appendix H in SI for the calculations, was added dropwise to obtain the $[Ni(NH_3)_6]^{2+}$ complex ion after setting the pH between 11.6-11.8. Then, the powdered supports were contacted with the impregnating solution and each suspension was left under stirring at 200 rpm for 1 h. Afterward, these suspensions were filtered and washed with deionized water four to five times. Impregnated materials were dried overnight at 90 °C.

For defining the heat treatment conditions of the impregnated solids, we performed a thermogravimetry analysis (TGA) for the fresh impregnated materials using a *Discovery 5500* (TA Instruments). To

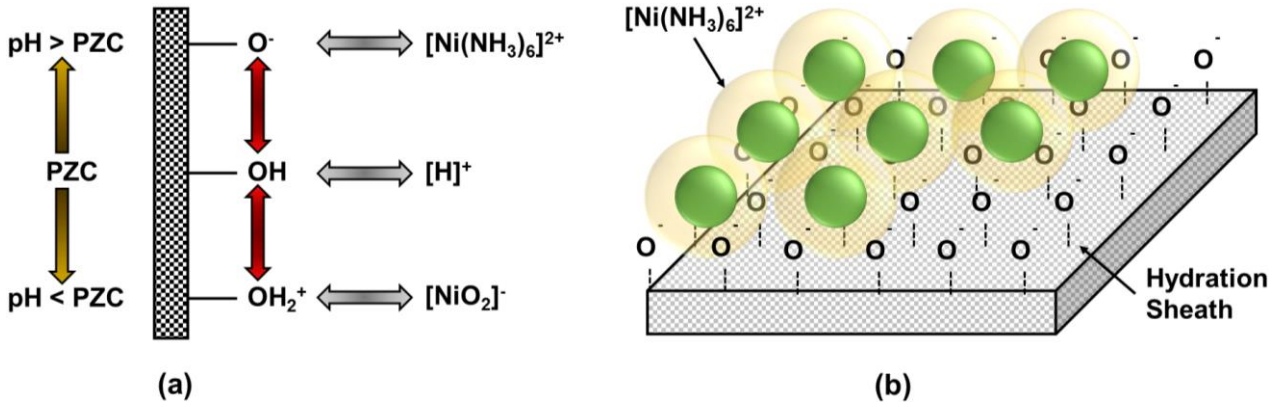

Figure 10. Electrostatic Adsorption Mechanism; (a) Surface Charging, Metal Adsorption and Proton Transfer. Adapted from reference,[159] and (b) Monolayer Coverage of Pt Anions with Hydration Sheath. Adapted from Regalbuto.[74]

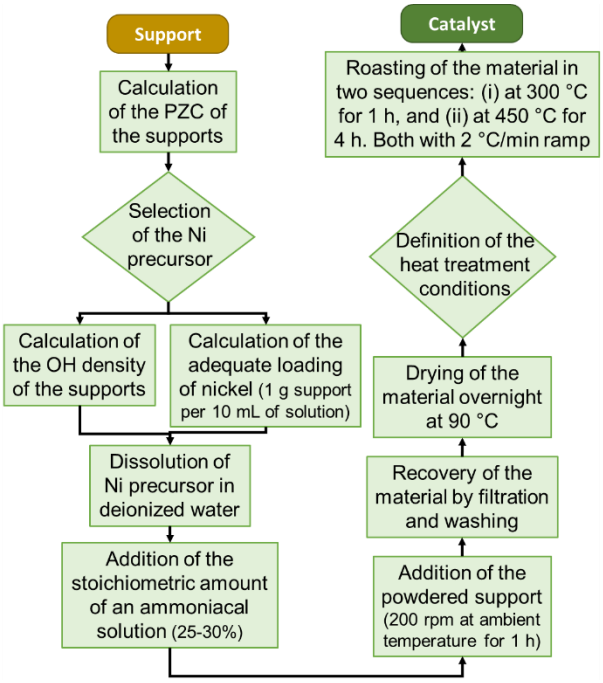

Figure 11. Flowchart for the catalyst preparation with the SEA method.

do this, about 10.0 mg of each sample were weighed and put into the instrument where they were heated from 25 °C to 800 °C by a ramp of 5 °C · min^{-1}, under an air flow (99.997%) of 25 mL · min^{-1}. The data were analyzed with the *Trios v4.4.0.41128* (TA Instruments) software. With this information (see SI), catalysts were roasted using two sequential heating stages: the first was by heating to 300 °C and holding this condition for 1 h. The second was by heating to 450 °C for 4 h. In each case, a 2 °C · min^{-1} ramp was used. Finally, catalysts synthesized by the above methods were named: Ni/Al_2O_3, Ni/SiO_2, Ni/H-Y, and Ni/H^+-YM, according to the used support.

For reference purposes, a material with the same nickel loading and supported over H^+-YM was prepared using the wetness impregnation method.[160] To do so, the same Ni precursor used before was dissolved in the necessary volume of water to keep the ratio of 1 g of support per 10 mL of solution. Then, the solution was contacted with the established amount of support to be impregnated. The mixture was stirred for 1 h and then left to rest for 18 h at room temperature. Subsequently, the excess water was dried overnight at 90 °C, and the recovered solid was thermally treated in the same way as it was made for the other catalysts. This catalyst was called Ni/H^+-YM(WI).

Characterization of the catalysts. The surface area, volume, and pore size distribution were determined for all catalysts from Ar physisorption tests, as mentioned in the **Determination of the surface area and porosity of the materials Section**. Likewise, the distribution of their surface hydroxyls was analyzed using the methods explained in the **Determination of the distribution of surface hydroxyls Section**. The surface acid sites were determined as mentioned in the **Determination of surface acid sites Section**. On the other hand, the total bulk loading of Ni was measured by flame atomic absorption spectrometry, where approximately 0.2000 g of each catalyst were subjected to an acid digestion process[161] with 1.5 mL of sulfuric acid (H_2SO_4, Merck, 65% v/v) added dropwise. Subsequently, the samples were treated with 2 mL of hydrofluoric acid (HF, Merck, 80%) at 80 °C for about 30 min. At this point, all sulfur trioxide fumes came out.[161] Finally, 100 mL of deionized water were added to the samples to complete the dissolution process. On the other hand, to qualitatively analyze whether nanoparticles of nickel formed inside the pores of the supports, normalized SSA_{BET} ($NSSA_{BET}$) values were calculated using Equation 2:[77–79]

$$NSSA_{BET} = \frac{SSA_{BET(catalyst)}}{SSA_{BET(support)}} \times (1 - x) \qquad (2)$$

Where, $SSA_{BET(catalyst)}$ is the BET specific surface area of the powder catalysts and x is the bulk weight fraction of Ni. The interpretation of this equation is that values close to 1 correspond to well dispersed phases that do not form nanoparticles causing pore blocking.[77,78]

Concentration of surface Ni. The concentration of surface Ni was determined by X-ray Photoelectron Spectroscopy. Measurements were carried out with the *XPS/ISS/UPS-A.Centeno* (SPECS) surface characterization platform, equipped with a PHOIBOS 150 2D-DLD energy analyzer. The spectra were recorded using a monochromatic Al Kα source (hυ=1486.6 eV) operated with 100 W and 12 kV. For the analyses, the samples were deposited on a carbon conductive tape which was mounted on a metallic sample holder. Samples were placed inside the instrument via its introduction chamber for outgassing and then moved to the analysis chamber which was at a base pressure of ca. 1×10^{-7} Pa. Spectra were recorded after setting the pass energy of the analyzer at 100 eV,

energy step equal to 1.000 eV, for recording general surveys and at 15 eV, energy step equal to 0.050 eV, for recording high-resolution spectra of specific core lines. The charge developed by the surface of the samples by the photoelectron emission process was compensated with an electron flood gun (FG 15/40-PS FG500) operated either between 1 and 10 eV or between 58 and 70 μA, as required for avoiding artificial chemical shifts and deformation of the recorded peaks. The following sequence of spectra was recorded: general spectrum, C 1s, O 1s, Na 1s, Si 2p + Al 2p, Ni 2p, N 1s, and C 1s again to check the stability of charge compensation as a function of time. Spectra were processed and analyzed with the Casa–XPS software (Casa Software Ltd.)[162] using the relative sensitivity factors (R.S.F) provided by the manufacturer. We used a Shirley-Tougaard type baseline. The binding energy (BE) scale was corrected by using the C- [C, H] component of the adventitious carbon peak at 284.8 eV as a reference. Samples of Ni/H^+-YM and Ni/H^+-YM(WI) were reduced with H_2 before analyses. This pre-treatment was carried out in a high-pressure cell (HPC). coupled with the XPS analysis chamber, hence allowing to analyze the samples directly after the applied treatments and avoiding contact with ambient air. The HPC has an IR heating system and operates at a maximum temperature and pressure of 800°C and 2 MPa, respectively. The general procedure was as follows: the samples were transferred from the introduction chamber to the HPC via the central linear vacuum line of the instrument. Then, samples were treated under H_2 flow (100 mL · min^{-1}) at 400 °C (heating rate: 5 °C · min^{-1}) and 0.1 MPa for 4 h. XPS spectra were recorded before and after reducing the samples in the HPC.

We tried to estimate the particle size of Ni using the model proposed by Kerkhof and Moulijn.[163] Unfortunately, the method did not work with our data due to the very low Ni loading of the materials and because Ni is a "light metal" compared with metals such as Rh, Pd, and Pt. The problem with the method was that its convergence could only be assured if the concentration of nickel was of at least 12.5 wt.%. We also tried to estimate the Ni dispersion and the Ni particle sizes via H_2 chemisorption, however, it was no possible due to the too low Ni loading (see Figure S43 in the SI).

Catalytic tests. Catalytic tests were carried out in a Catatest provided with a high-pressure fixed-bed continuous flow reactor.[23–25,27,29,52,164] The reactor was packed with the catalyst. Prior to the latter, the catalytic powders were pelletized, ground, and sieved to obtain particles with diameters ranging from 300 to 600 μm. For the catalytic tests, ca. 0.5000 g were dried in situ under an N_2 flow (100 mL · min^{-1}) at 120 °C for 1 h. Afterwards, the catalyst was activated during 4 h using a H_2 volumetric flow rate of 100 mL · min^{-1} at atmospheric pressure and 400 °C. After activation, reactants were fed into the reactor at a volumetric flow rate of 30 mL · h^{-1}. Then, the reactor pressure was increased with H_2 to 5 MPa and the liquid feed was pumped up to the reactor. A hydrogen/(liquid feed) rate ratio of 260 NL · L^{-1} was fixed for the experiments. Reaction temperatures were programmed to start at 300 °C, to stabilize the catalyst. The reaction feedstock accounted for the following compounds employed either individually or in blends: dibenzothiophene (DBT, Sigma-Aldrich, 98%), as a model sulfur compound. Dodecane ($C_{12}H_{26}$, Sigma-Aldrich, 99%) was used as an internal standard for chromatography, hexadecane ($C_{16}H_{34}$, Sigma-Aldrich, 99%) was used to follow the cracking reactions of aliphatic compounds, and cyclohexane (C_6H_{12}, Sigma-Aldrich, 99.8%) was used as solvent. For all tests, 2.2 wt.% DBT were put into the liquid feed.

The identification and quantification of the liquid reaction products were made by the gas chromatography (GC) and GC mass spectroscopy (GC-MS) techniques. Gas chromatography analyses were performed with a HP 6890 chromatograph equipped with an FID detector and an automatic injector. An HP-1 column (Agilent J&W, 100 m×0.25 mm×0.5 μm) was used for both GC and GC-MS. The analysis conditions were as follows: the GC oven temperature was programmed from 90 to 180 °C (15 min) at 30 °C · min^{-1}, then to 260 °C (10 min) using a temperature ramp of 30 °C · min^{-1}. We used a H_2 flow of 50 mL · min^{-1}, an air flow of 500 mL · min^{-1}, and helium (Linde Colombia S.A, 99.99%) as carrier gas, with 19 cm · s^{-1} linear velocity (1.1 mL · min^{-1}, at constant flow). The compounds in each sample were identified by comparing their retention times with those of standards, and the quantification was carried out using calibration curves. Some chromatograms are shown in Figures S35-S40.

In general, catalytic results were expressed in terms of reactants conversion (%X_i), and product yield (%Y_j) percentages, as follows:

$$\%X_i = \frac{n_{i_{initial}} - n_{i_{final}}}{n_{i_{initial}}} \times 100 \quad (3)$$

Where, $n_{i_{initial}}$ and $n_{i_{final}}$ are the initial and final moles of the reagent (*i*), respectively.

$$\%Y_j = \frac{n_j}{n_{i_{initial}}} \times 100 \quad (4)$$

Where, n_j are the moles of the product *j*.

These yields were used to analyze the catalytic results in terms of apparent kinetic pseudo-constants for the formation of products using the following expression:

$$k_j = -\frac{F_{DBT}}{W_{Cat}} \times \ln(1 - Y_j) \quad (5)$$

Where, $k_j(\mu mol \cdot g^{-1} \cdot h^{-1})$ is the pseudo-first order kinetic constants for the formation of the product *j*, F_{DBT} is the DBT molar flow (mol · h^{-1}), and W_{Cat} is the catalyst weight (g).

Supporting Information

The Supporting Information contains the results for the textural and acidity properties of the supports and the catalysts, the surface compositions of the catalysts, and chromatograms of the catalytic results. The authors have cited additional references within the Supporting Information.[165–172] [173–182] [183–187]

Acknowledgements

Acknowledgements. Authors thank *Agencia Nacional de Hidrocarburos* (ANH) and MinCiencias for funding within the frame of the project 1102-847-69842: "*Desarrollo de una estrategia catalítica para un proceso de in-situ upgrading acoplado con procesos de combustión in-situ para optimizar la producción y mejorar la calidad de crudos pesados y extra-pesados colombianos por reacciones de transferencia de hidrógeno*". Authors also thank ECOPETROL S.A. for the specific science and technology cooperation agreement no. 3044679.

Keywords: dibenzothiophene • hydrodesulfurization • micro-mesostructured zeolite • nickel • strong electrostatic adsorption

References

[1] H. Alboudwarej, J. Felix, S. Taylor, R. Badry, C. Bremner, B. Brough, C. Skeates, A. Baker, D. Palmer, K. Pattison, M. Beshry, P. Krawchuk, G. Brown, R. Calvo, J. A. C. Triana, R. Hathcock, K. Koerner, T. Hughes, D. Kundu, J. L. De Cárdenas, C. West, *Oilf. Rev.* **2006**, *18*, 34–53.

[2] M. M. Ramírez-Corredores, A. P. Borole, in *Stud. Surf. Sci. Catal.*, Elsevier, **2007**, pp. 9–63.

[3] P. T. Vasudevan, J. L. G. Fierro, *Catal. Rev.* **1996**, *38*, 161–188.

[4] A. Tanimu, K. Alhooshani, *Energy & Fuels* **2019**, *33*, 2810–2838.

[5] T. A. Saleh, *Trends Environ. Anal. Chem.* **2020**, *25*, e00080.

[6] T.-Y. Cui, A. Rajendran, H.-X. Fan, J. Feng, W.-Y. Li, *Ind. Eng. Chem. Res.* **2021**, *60*, 3295–3323.

[7] U. EPA, "Sulfur Dioxide (SO2) Pollution," can be found under https://www.epa.gov/so2-pollution/sulfur-dioxide-basics, **n.d.**

[8] Y. Van Fan, S. Perry, J. J. Klemeš, C. T. Lee, *J. Clean. Prod.* **2018**, *194*, 673–684.

[9] G. Valavarasu, B. Ramachandrarao, in *Catal. Clean Energy Environ. Sustain.*, Springer International Publishing, Cham, **2021**, pp. 1–33.

[10] R. G. Leliveld, S. E. Eijsbouts, *Catal. Today* **2008**, *130*, 183–189.

[11] F. Parlevliet, S. Eijsbouts, *Catal. Today* **2008**, *130*, 254–264.

[12] S. S. Bello, C. Wang, M. Zhang, H. Gao, Z. Han, L. Shi, F. Su, G. Xu, *Energy & Fuels* **2021**, *35*, 10998–11016.

[13] S. Mahapatra, D. Kumar, B. Singh, P. K. Sachan, *Energy Nexus* **2021**, *4*, 100036.

[14] J. D. Benck, Z. Chen, L. Y. Kuritzky, A. J. Forman, T. F. Jaramillo, *ACS Catal.* **2012**, *2*, 1916–1923.

[15] A. Bähr, H. Petersen, H. Tüysüz, *ChemCatChem* **2021**, *13*, 3824–3835.

[16] E. M. Morales-Valencia, O. J. Vargas-Montañez, P. A. Monroy-García, L. G. Avendaño-Barón, E. A. Quintero-Quintero, C. Elder-Bueno, A. Y. Santiago-Guerrero, V. G. Baldovino-Medrano, *J. Catal.* **2021**, *404*, 204–209.

[17] J. Díaz de León, C. Ramesh Kumar, J. Antúnez-García, S. Fuentes-Moyado, *Catalysts* **2019**, *9*, 87.

[18] D. Duayne Whitehurst, T. Isoda, I. Mochida, in *Adv. Catal.*, **1998**, pp. 345–471.

[19] H. Wang, R. Prins, *J. Catal.* **2008**, *258*, 153–164.

[20] S. Jiang, S. Ding, Y. Zhou, S. Yuan, X. Geng, Z. Cao, *Int. J. Mol. Sci.* **2023**, *24*, 3044.

[21] X. Zhou, X. Li, R. Prins, J. Lv, A. Wang, Q. Sheng, *J. Catal.* **2021**, *394*, 167–180.

[22] M. Houalla, N. K. Nag, A. V. Sapre, D. H. Broderick, B. C. Gates, *AIChE J.* **1978**, *24*, 1015–1021.

[23] V. G. Baldovino-Medrano, A. Centeno, S. A. Giraldo, *Ciencia, Tecnol. y Futur.* **2010**, *4*, 91–99.

[24] E. M. Morales-Valencia, C. O. Castillo-Araiza, S. A. Giraldo, V. G. Baldovino-Medrano, *ACS Catal.* **2018**, *8*, 3926–3942.

[25] V. G. Baldovino-Medrano, P. Eloy, E. M. Gaigneaux, S. A. Giraldo, A. Centeno, *J. Catal.* **2009**, *267*, 129–139.

[26] M. Egorova, *J. Catal.* **2004**, *225*, 417–427.

[27] V. G. Baldovino-Medrano, S. A. Giraldo, A. Centeno, *Inf. Tecnol.* **2009**, *20*, 3–10.

[28] M. Egorova, R. Prins, *J. Catal.* **2006**, *241*, 162–172.

[29] V. G. Baldovino-Medrano, S. A. Giraldo, A. Centeno, *Fuel* **2010**, *89*, 1012–1018.

[30] F. Bataille, J. L. Lemberton, P. Michaud, G. Pérot, M. Vrinat, M. Lemaire, E. Schulz, M. Breysse, S. Kasztelan, *J. Catal.* **2000**, *191*, 409–422.

[31] M. J. B. Souza, A. M. Garrido Pedrosa, J. A. Cecilia, A. M. Gil-Mora, E. Rodríguez-Castellón, *Catal. Commun.* **2015**, *69*, 217–222.

[32] J. Wang, W.-Z. Li, G. Perot, J. L. Lemberton, C.-Y. Yu, C. Thomas, Y.-Z. Zhang, in *Stud. Surf. Sci. Catal.*, **1997**, pp. 171–178.

[33] S. A. Giraldo, M. H. Pinzón, A. Centeno, *Catal. Today* **2008**, *133–135*, 239–243.

[34] L. I. Meriño, A. Centeno, S. A. Giraldo, *Appl. Catal. A Gen.* **2000**, *197*, 61–68.

[35] C. B. Rasrendra, E. G. Maulidanti, S. E. P. Darlismawantyani, N. Nurdini, W. Rustyawan, Subagjo, G. T. M. Kadja, *Case Stud. Chem. Environ. Eng.* **2023**, *8*, 100427.

[36] C. B. Rasrendra, E. G. Maulidanti, S. E. P. Darlismawantyani, N. Nurdini, W. Rustyawan, Subagjo, G. T. M. Kadja, *Case Stud. Chem. Environ. Eng.* **2023**, *8*, 100427.

[37] D. Pérez-Martínez, S. A. Giraldo, A. Centeno, *Appl. Catal. A Gen.* **2006**, *315*, 35–43.

[38] J. A. Medina Cervantes, J. N. Díaz de León, S. Fuentes Moyado, G. Alonso-Núñez, *Mol. Catal.* **2023**, *547*, 113399.

[39] K. Yu, W.-M. Kong, Z. Zhao, A.-J. Duan, L. Kong, X.-L. Wang, *Pet. Sci.* **2023**, DOI 10.1016/j.petsci.2023.08.007.

[40] P. Zheng, C. Xiao, Z. Cao, Y. Shi, G. Wang, A. Duan, C. Xu, *Chem. Eng. Sci.* **2021**, *231*, 116311.

[41] S. Rangarajan, M. Mavrikakis, *ACS Catal.* **2016**, *6*, 2904–2917.

[42] B. Hinnemann, P. G. Moses, J. K. Nørskov, *J. Phys. Condens. Matter* **2008**, *20*, 064236.

[43] E. Krebs, A. Daudin, P. Raybaud, *Oil Gas Sci. Technol. - Rev. l'IFP* **2009**, *64*, 707–718.

[44] P. Raybaud, *Appl. Catal. A Gen.* **2007**, *322*, 76–91.

[45] V. H. . de Beer, J. . Duchet, R. Prins, *J. Catal.* **1981**, *72*, 369–372.

[46] Z. Yu, L. E. Fareid, K. Moljord, E. A. Blekkan, J. C. Walmsley, D. Chen, *Appl. Catal. B Environ.* **2008**, *84*, 482–489.

[47] T. . Pecoraro, R. . Chianelli, *J. Catal.* **1981**, *67*, 430–445.

[48] T. Kabe, W. Qian, Y. Hirai, L. Li, A. Ishihara, *J. Catal.* **2000**, *190*, 191–198.

[49] M. H. Pinzón, A. Centeno, S. A. Giraldo, *Appl. Catal. A Gen.* **2006**, *302*, 118–126.

[50] V. G. Baldovino-Medrano, S. A. Giraldo, A. Centeno, *Fuel* **2008**, *87*, 1917–1926.

[51] V. G. Baldovino-Medrano, S. A. Giraldo, A. Centeno, *J. Mol. Catal. A Chem.* **2009**, *301*, 127–133.

[52] V. G. Baldovino-Medrano, S. A. Giraldo, A. Centeno, *Catal. Letters* **2009**, *130*, 291–295.
[53] V. G. Baldovino-Medrano, P. Eloy, E. M. Gaigneaux, S. A. Giraldo, A. Centeno, *Catal. Today* **2010**, *150*, 186–195.
[54] M. Ramírez, R. Barajas, S. A. Giraldo, *Rev. ION* **2012**, *25*, 67–72.
[55] E. Yik, E. Iglesia, *J. Catal.* **2018**, *368*, 411–426.
[56] H. Schweiger, P. Raybaud, H. Toulhoat, *J. Catal.* **2002**, *212*, 33–38.
[57] J. Zhao, Y. Chai, B. Liu, Y. Liu, Y. Liu, C. Liu, *Catal. Commun.* **2019**, *119*, 6–10.
[58] M. Trueba, S. P. Trasatti, *Eur. J. Inorg. Chem.* **2005**, *2005*, 3393–3403.
[59] D. L. Trimm, A. Stanislaus, *Appl. Catal.* **1986**, *21*, 215–238.
[60] V. H. J. De Beer, T. H. M. Van Sint Fiet, G. H. A. M. Van Der Steen, A. C. Zwaga, G. C. A. Schuit, *J. Catal.* **1974**, *35*, 297–306.
[61] R. Burch, A. Collins, *J. Catal.* **1986**, *97*, 385–389.
[62] B. Pawelec, R. Mariscal, J. L. . Fierro, A. Greenwood, P. . Vasudevan, *Appl. Catal. A Gen.* **2001**, *206*, 295–307.
[63] C. S. Brooks, D. G. Pilney, *Surf. Technol.* **1979**, *9*, 119–133.
[64] N. Davidova, P. Kovacheva, D. Shopov, in *Stud. Surf. Sci. Catal.*, Elsevier Science Publishers B.V., **1985**, pp. 659–665.
[65] P. Kovacheva, N. Davidova, J. Nováková, *Zeolites* **1991**, *11*, 54–58.
[66] W. J. J. Welters, T. I. Korányi, V. H. J. de Beer, R. A. van Santen, in *Stud. Surf. Sci. Catal.*, **1993**, pp. 1931–1934.
[67] R. Cid, F. J. Gil Llambías, M. González, A. López Agudo, *Catal. Letters* **1994**, *24*, 147–157.
[68] D. Li, A. Nishijima, D. E. Morris, G. D. Guthrie, *J. Catal.* **1999**, *188*, 111–124.
[69] D. Li, A. Nishijima, D. E. Morris, **1999**, *348*, 339–348.
[70] C. S. Brooks, *Surf. Technol.* **1979**, *9*, 135–146.
[71] C. S. Brooks, *Surf. Technol.* **1980**, *10*, 379–397.
[72] A. Sites, in *Stud. Surf. Sci. Catal.*, **1989**, pp. 72–90.
[73] B. Imelik, C. Naccache, G. Coudurier, Y. Ben Taarit, J. . Vedrine, *Studies in Surface Science and Catalysis*, Elsevier, **1985**.
[74] J. R. Regalbuto, *Catalyst Preparation: Science and Engineering.*, CRC PRESS, Boca Raton, **2006**.
[75] H. R. Cho, J. R. Regalbuto, *Catal. Today* **2015**, *246*, 143–153.
[76] S. Mhadmhan, P. Natewong, N. Prasongthum, C. Samart, P. Reubroycharoen, *Catalysts* **2018**, *8*, 319.
[77] M. S. Hernández-Maya, C. B. Espinosa-Lobo, R. Cabanzo-Hernández, E. Mejía-Ospino, V. G. Baldovino-Medrano, *Mol. Catal.* **2022**, *520*, 112158.
[78] P. E. Boahene, K. K. Soni, A. K. Dalai, J. Adjaye, *Appl. Catal. A Gen.* **2011**, *402*, 31–40.
[79] J. R. Restrepo-Garcia, G. E. Ramírez, V. G. Baldovino-Medrano, *Catal. Letters* **2018**, *148*, 621–641.
[80] C. Contescu, J. Jagiello, J. A. Schwarz, *Stud. Surf. Sci. Catal.* **1995**, *91*, 237–252.
[81] F. Machuca, S. G. de León, A. Centeno, J. L. G. Fierro, *J. Colloid Interface Sci.* **2001**, *237*, 290–293.
[82] Y. H. Kang, X. Y. Wei, G. H. Liu, Y. Gao, Y. J. Li, X. R. Ma, Z. F. Zhang, Z. M. Zong, *Fuel* **2020**, *269*, 117326.
[83] Y. H. Kang, X. Y. Wei, X. Q. Zhang, Y. J. Li, G. H. Liu, X. R. Ma, X. Li, H. C. Bai, Z. N. Li, H. J. Yan, Z. M. Zong, *Renew. Energy* **2021**, *173*, 876–885.
[84] Y. H. Kang, X. Y. Wei, J. Li, H. tao Jin, T. Li, C. Y. Lu, X. R. Ma, Z. M. Zong, *Fuel* **2021**, *287*, 119396.
[85] W. Huang, Q. Wei, Y. Zhou, X. Liu, M. Liu, P. Zhang, Z. Xu, Z. Yu, X. Wang, H. Liu, *Catal. Today* **2023**, *407*, 135–145.
[86] National Institute of Standards and Technology (NIST), "NIST X-ray Photoelectron Spectroscopy Database, NIST Standard Reference Database Number 20," DOI 10.18434/T4T88K, **2000**.
[87] P. Dufresne, E. Payen, J. Grimblot, J. P. Bonnelle, *J. Phys. Chem.* **1981**, *85*, 2344–2351.
[88] T. Long-Xiang, Z. Feng-Mei, Z. Lu-Bin, *React. Kinet. Catal. Lett.* **1996**, *57*, 99–104.
[89] J. T. García-Sánchez, I. D. Mora-Vergara, D. R. Molina-Velasco, J. A. Henao-Martínez, V. G. Baldovino-Medrano, *ChemCatChem* **2021**, *13*, 3713–3730.
[90] M. I. Vázquez, A. Corma, V. Fornés, *Zeolites* **1986**, *6*, 271–274.
[91] I. Eswaramoorthi, N. Lingappan, *Catal. Letters* **2003**, *87*, 133–142.
[92] Z. R. Ismagilov, S. A. Yashnik, A. N. Startsev, A. I. Boronin, A. I. Stadnichenko, V. V. Kriventsov, S. Kasztelan, D. Guillaume, M. Makkee, J. A. Moulijn, *Catal. Today* **2009**, *144*, 235–250.
[93] W. Fu, L. Zhang, T. Tang, Q. Ke, S. Wang, J. Hu, G. Fang, J. Li, F. S. Xiao, *J. Am. Chem. Soc.* **2011**, *133*, 15346–15349.
[94] T. Isoda, S. Nagao, X. Ma, Y. Korai, I. Mochida, *Energy and Fuels* **1996**, *10*, 1078–1082.
[95] K. Kaneda, T. Wada, S. Murata, M. Nomura, *Energy & Fuels* **1998**, *12*, 298–303.
[96] T. Isoda, Y. Takase, K. Kusakabe, S. Morooka, *Energy & Fuels* **2000**, *14*, 585–590.
[97] F. Wang, K. Han, L. Xu, H. Yu, W. Shi, *Ind. Eng. Chem. Res.* **2021**, *60*, 3324–3333.
[98] J. M. Jehng, C. M. Chen, *Catal. Letters* **2001**, *77*, 147–154.
[99] A. Gil, A. Díaz, L. M. Gandía, M. Montes, *Appl. Catal. A, Gen.* **1994**, *109*, 167–179.
[100] J. L. Ewbank, L. Kovarik, F. Z. Diallo, C. Sievers, *Appl. Catal. A Gen.* **2015**, *494*, 57–67.
[101] T. I. Korányi, M. Dobrovolszky, T. Koltai, K. Matusek, Z. Paál, P. Tétényi, *Fuel Process. Technol.* **1999**, *61*, 55–71.
[102] Q. Wei, P. Zhang, X. Liu, W. Huang, X. Fan, Y. Yan, R. Zhang, L. Wang, Y. Zhou, *Front. Chem.* **2020**, *8*, 1–8.
[103] T. Numaguchi, H. Eida, K. Shoji, *Int. J. Hydrogen Energy* **1997**, *22*, 1111–1115.
[104] Z. D. Huang, W. Bensch, A. Lotnyk, L. Kienle, S. Fuentes, J. Bocarando, G. Alonso, C. Ornelas, *J. Mol. Catal. A Chem.* **2010**, *323*, 45–51.
[105] L. Coulier, V. H. J. De Beer, J. A. R. Van Veen, J. W. Niemantsverdriet, *J. Catal.* **2001**, *197*, 26–33.
[106] I. Bezverkhyy, O. V. Safonova, P. Afanasiev, J. P. Bellat, *J. Phys. Chem. C* **2009**, *113*, 17064–17069.

[107] N. Kunisada, K. H. Choi, Y. Korai, I. Mochida, *Appl. Catal. A Gen.* **2004**, *260*, 185–190.
[108] I. Bezverkhyy, A. Ryzhikov, G. Gadacz, J. P. Bellat, *Catal. Today* **2008**, *130*, 199–205.
[109] X. Gao, H. Mao, M. Lu, J. Yang, B. Li, *Microporous Mesoporous Mater.* **2012**, *148*, 25–33.
[110] S. Aslam, F. Subhan, Z. Yan, W. Xing, J. Zeng, Y. Liu, M. Ikram, S. Rehman, R. Ullah, *Microporous Mesoporous Mater.* **2015**, *214*, 54–63.
[111] S. Aslam, F. Subhan, Z. Yan, Z. Liu, R. Ullah, U. J. Etim, W. Xing, *Chem. Eng. J.* **2017**, *321*, 48–57.
[112] Y. Zhao, W. Zhao, Y. Xiao, Q. Zhao, C. Li, X. Dong, S. Lu, *Fuel* **2023**, *334*, 126657.
[113] R. R. Chianelli, *Oil Gas Sci. Technol.* **2006**, *61*, 503–513.
[114] R. P. Ren, X. W. Liu, Z. J. Zuo, Y. K. Lv, *RSC Adv.* **2015**, *5*, 55372–55382.
[115] J. M. H. Lo, T. Ziegler, P. D. Clark, *J. Phys. Chem. C* **2011**, *115*, 1899–1910.
[116] C. Arrouvel, H. Toulhoat, M. Breysse, P. Raybaud, *J. Catal.* **2004**, *226*, 260–272.
[117] L. P. A. F. Elst, S. Eijsbouts, A. D. van Langeveld, J. A. Moulijn, *J. Catal.* **2000**, *196*, 95–103.
[118] B. M. Vogelaar, P. Steiner, A. Dick van Langeveld, S. Eijsbouts, J. A. Moulijn, *Appl. Catal. A Gen.* **2003**, *251*, 85–92.
[119] R. Hamidi, R. Khoshbin, R. Karimzadeh, *Adv. Powder Technol.* **2021**, *32*, 524–534.
[120] N. T. Ramírez-Marquez, D. J. Pérez-Martínez, C.-A. Trujillo, *Microporous Mesoporous Mater.* **2023**, *360*, 112700.
[121] M. Umar, I. Abdulazeez, A. Tanimu, S. A. Ganiyu, K. Alhooshani, *J. Environ. Chem. Eng.* **2021**, *9*, 106738.
[122] D. A. Solís-Casados, T. Klimova, R. Cuevas, J. Ramírez, A. López-Agudo, *Catal. Today* **2004**, *98*, 201–206.
[123] J. Ren, A. Wang, X. Li, Y. Chen, H. Liu, Y. Hu, *Appl. Catal. A Gen.* **2008**, *344*, 175–182.
[124] W. Han, H. Nie, X. Long, M. Li, Q. Yang, D. Li, *Catal. Today* **2017**, *292*, 58–66.
[125] W. Zhou, A. Zhou, Y. Zhang, C. Zhang, Z. Chen, L. Liu, Y. Zhou, Q. Wei, X. Tao, *J. Catal.* **2019**, *374*, 345–359.
[126] Z. Cao, X. Zhang, R. Guo, S. Ding, P. Zheng, J. Fan, J. Mei, C. Xu, A. Duan, *Chem. Eng. J.* **2020**, *400*, 125886.
[127] T. Klimova, L. Lizama, J. C. Amezcua, P. Roquero, E. Terrés, J. Navarrete, J. M. Domínguez, *Catal. Today* **2004**, *98*, 141–150.
[128] S. Song, X. Zhou, A. Duan, Z. Zhao, K. Chi, M. Zhang, G. Jiang, J. Liu, J. Li, X. Wang, *Microporous Mesoporous Mater.* **2016**, *226*, 510–521.
[129] H. Adkins, H. I. Cramer, *J. Am. Chem. Soc.* **1930**, *52*, 4349–4358.
[130] L. Nichols, in *Org. Chem.*, LibreTexts, **2022**, pp. 58–62.
[131] A. Sachse, A. Grau-Atienza, E. O. Jardim, N. Linares, M. Thommes, J. García-Martínez, *Cryst. Growth Des.* **2017**, *17*, 4289–4305.
[132] M. Liu, Y. Ren, J. Wu, Y. Wang, J. Chen, X. Lei, X. Zhu, *Microporous Mesoporous Mater.* **2020**, *293*, DOI 10.1016/j.micromeso.2019.109800.
[133] J. Park, J. R. Regalbuto, *J. Colloid Interface Sci.* **1995**, *175*, 239–252.
[134] M. Kosmulski, *Compilation of PZC and IEP of Sparingly Soluble Metal Oxides and Hydroxides from Literature*, **2009**.
[135] N. Fiol, I. Villaescusa, *Environ. Chem. Lett.* **2009**, *7*, 79–84.
[136] M. Pashai Gatabi, H. Milani Moghaddam, M. Ghorbani, *J. Mol. Liq.* **2016**, *216*, 117–125.
[137] S. Brunauer, P. H. Emmett, E. Teller, *J. Am. Chem. Soc.* **1938**, *60*, 309–319.
[138] J. Rouquerol, F. Rouquerol, P. Llewellyn, G. Maurin, K. S. W. Sing, *Adsorption by Powders and Porous Solids: Principles, Methodology and Applications: Second Edition*, **2013**.
[139] B. C. Lippens, J. H. de Boer, *J. Catal.* **1965**, *4*, 319–333.
[140] W. D. Harkins, G. Jura, *J. Chem. Phys.* **1943**, *11*, 431–432.
[141] W. D. Harkins, G. Jura, *J. Am. Chem. Soc.* **1944**, *66*, 1366–1373.
[142] M. Jaroniec, M. Kruk, J. P. Oliver, S. Koch, *Stud. Surf. Sci. Catal.* **2000**, *128*, 71–80.
[143] E. P. Barrett, L. G. Joyner, P. P. Halenda, *J. Am. Chem. Soc.* **1951**, *73*, 373–380.
[144] R. Cosentino, "BJH Pore Volume and Area Distributions," can be found under https://notebook.community/RJC0514/micromeritics/documentation/BJH, **2017**.
[145] C. Contescu, J. Jagiełło, J. A. Schwarz, *Langmuir* **1993**, *9*, 1754–1765.
[146] D. J. Pérez Martínez, G. A. A. Quiroga, S. A. G. Duarte, A. C. Hurtado, *Rev. Fac. Ing.* **2011**, 23–30.
[147] I. D. Mora-Vergara, L. Hernández Moscoso, E. M. Gaigneaux, S. A. Giraldo, V. G. Baldovino-Medrano, *Catal. Today* **2018**, *302*, 125–135.
[148] J. Datka, *J. Chem. Soc. Faraday Trans. 1 Phys. Chem. Condens. Phases* **1980**, *76*, 2437–2447.
[149] J. Datka, B. Gil, A. Kubacka, *Zeolites* **1996**, *17*, 428–433.
[150] E. Selli, L. Forni, **1999**, *31*, 129–140.
[151] C. A. Emeis, *J. Catal.* **1993**, *141*, 347–354.
[152] T. R. Hughes, H. M. White, *Phys. Chem.* **1967**, *71*, 2192–2201.
[153] V. Zholobenko, C. Freitas, M. Jendrlin, P. Bazin, A. Travert, F. Thibault-Starzyk, *J. Catal.* **2020**, *385*, 52–60.
[154] F. Thibault-Starzyk, B. Gil, S. Aiello, T. Chevreau, J. P. Gilson, *Microporous Mesoporous Mater.* **2004**, *67*, 107–112.
[155] S. Khabtou, T. Chevreau, J. C. Lavalley, *Microporous Mater.* **1994**, *3*, 133–148.
[156] J. W. Harris, M. J. Cordon, J. R. Di Iorio, J. C. Vega-Vila, F. H. Ribeiro, R. Gounder, *J. Catal.* **2016**, *335*, 141–154.
[157] I. S. Pieta, M. Ishaq, R. P. K. Wells, J. A. Anderson, *Appl. Catal. A Gen.* **2010**, *390*, 127–134.
[158] M. Guisnet, P. Ayrault, C. Coutanceau, M. F. Alvarez, J. Datka, *J. Chem. Soc. - Faraday Trans.* **1997**, *93*, 1661–1665.
[159] H. Cho, The Rational Synthesis of Supported Noble Single Or Bimetallic Catalysts by Electrostatic Adsorption, University of South Carolina, **2013**.

[160] J. R. A. Sietsma, A. Jos van Dillen, P. E. de Jongh, K. P. de Jong, *Application of Ordered Mesoporous Materials as Model Supports to Study Catalyst Preparation by Impregnation and Drying*, Elsevier Masson SAS, **2006**.
[161] D. W. B. Westerman, I. E. Ruffio, N. R. Foster, *Anal. Chim. Acta* **1980**, *117*, 285–291.
[162] N. Fairley, V. Fernandez, M. Richard-Plouet, C. Guillot-Deudon, J. Walton, E. Smith, D. Flahaut, M. Greiner, M. Biesinger, S. Tougaard, D. Morgan, J. Baltrusaitis, *Appl. Surf. Sci. Adv.* **2021**, *5*, 100112.
[163] F. P. J. M. Kerkhof, J. A. Moulijn, *J. Phys. Chem.* **1979**, *83*, 1612–1619.
[164] E. M. Morales, I. D. Mora, S. A. Giraldo, *Rev. ION* **2011**, *24*, 53–60.
[165] M. Kosmulski, *Surf. Charg. Points Zero Charg.* **2009**, 1–1065.
[166] R. P. Abendroth, *J. Colloid Interface Sci.* **1970**, *34*, 591–596.
[167] D. E. Yates, T. W. Healy, *J. Colloid Interface Sci.* **1976**, *55*, 9–19.
[168] J. S. Noh, J. A. Schwarz, *J. Colloid Interface Sci.* **1989**, *103*, 157–164.
[169] M. R. Das, O. P. Sahu, P. C. Borthakur, S. Mahiuddin, *Colloids Surfaces A Physicochem. Eng. Asp.* **2004**, *237*, 23–31.
[170] C. Contescu, A. Contescu, J. A. Schwarz, *J. Phys. Chem.* **1994**, *98*, 4327–4335.
[171] R. Greenwood, *Adv. Colloid Interface Sci.* **2003**, *106*, 55–81.
[172] M. Kosmulski, *Pr. Nauk. Inst. Górnictwa Politech. Wrocławskiej, Konf.* **2000**, *31*, 1–5.
[173] G. Busca, P. J. F. Kennedy, *Microporous Mesoporous Mater.* **2017**, *254*, 3–16.
[174] R. H. Lopez, Caracterización de Medios Porosos y Procesos Percolativos y de Transporte, Universidad Nacional de San Luis, **2004**.
[175] M. Thommes, K. Kaneko, A. V. Neimark, J. P. Olivier, F. Rodriguez-Reinoso, J. Rouquerol, K. S. W. Sing, *Physisorption of Gases, with Special Reference to the Evaluation of Surface Area and Pore Size Distribution (IUPAC Technical Report)*, **2015**.
[176] J. M. Martín Martínez, *Adsorción Física de Gases y Vapores Por Carbones*, Universidad De Alicante, **n.d.**
[177] N. L. Dias Filho, D. R. do Carmo, F. Newton Luiz Dias, C. Devaney Ribeiro do, *Encycl. Surf. Colloid Sci. Second Ed.* **2006**, *1*, 209–228.
[178] Y. Duval, J. A. Mielczarski, O. S. Pokrovsky, E. Mielczarski, J. J. Ehrhardt, *J. Phys. Chem. B* **2002**, *106*, 2937–2945.
[179] H. Knözinger, P. Ratnasamy, *Catal. Rev.* **1978**, *17*, 31–70.
[180] L. D. Borges, J. L. de Macedo, *Microporous Mesoporous Mater.* **2016**, *236*, 85–93.
[181] M. Gackowski, K. Tarach, Kuterasiński, J. Podobiński, S. Jarczewski, P. Kuśtrowski, J. Datka, *Microporous Mesoporous Mater.* **2018**, *263*, 282–288.
[182] V. G. Baldovino-Medrano, V. Niño-Celis, R. Isaacs Giraldo, *J. Chem. Eng. Data* **2023**, *68*, 2512–2528.
[183] R. Zhang, S. Xu, D. Raja, N. B. Khusni, J. Liu, J. Zhang, S. Abdulridha, H. Xiang, S. Jiang, Y. Guan, Y. Jiao, X. Fan, *Microporous Mesoporous Mater.* **2019**, *278*, 297–306.
[184] G. Gran, *Analyst* **1952**, *77*, 661–671.
[185] F. Ingman, E. Still, *Talanta* **1966**, *13*, 1431–1442.
[186] C. Ardila-Suárez, A. M. Díaz-Lasprilla, L. A. Díaz-Vaca, P. B. Balbuena, V. G. Baldovino-Medrano, G. E. Ramírez-Caballero, *CrystEngComm* **2019**, *21*, 3014–3030.
[187] J. B. Condon, *Surface Area and Porosity Determinations by Physisorption: Measurements and Theory*, Elsevier, **2006**.